

1 **One-year Continuous Observations of Near-Surface Atmospheric**
2 **Water Vapor Stable Isotopes at Matara, Sri Lanka**

3 Yuqing Wu ^{1,2}, Jing Gao ^{1,3,*}, Aibin Zhao ¹, Xiaowei Niu ¹, Yigang Liu ¹,
4 ², Disna Ratnasekera ^{4,5}, Tilak Priyadarshana Gamage ⁶, Amarasinghe
5 Hewage Ruwan Samantha ⁶

6 *1 State Key Laboratory of Tibetan Plateau Earth System, Resources and Environment,*
7 *Institute of Tibetan Plateau Research, Chinese Academy of Sciences, Beijing 100101,*
8 *China*

9 *2 University of the Chinese Academy of Sciences, Beijing, 100049, China*

10 *3 Lanzhou University, Lanzhou 733000, China*

11 *4 China-Sri Lanka Joint Center for Education & Research, Guangzhou 510301, China*

12 *5 Department of Agricultural Biology, Faculty of Agriculture, University of Ruhuna,*
13 *Matara 81000, Sri Lanka*

14 *6 Faculty of Fisheries and Marine Sciences & Technology, University of Ruhuna,*
15 *Matara 81000, Sri Lanka*

16 ** Corresponding author: Jing Gao (gaojing@itpcas.ac.cn)*

17

18 **Abstract:**

19 Atmospheric water vapor stable isotopes are crucial for understanding
20 hydrological cycle processes under climate change. This study presents the results from
21 a year-long in-situ monitoring of atmospheric water vapor stable isotopes ($\delta^{18}\text{O}$, δD) at
22 Matara, Sri Lanka, from March 2020 to February 2021 to assess how oceanic sources
23 and moisture transport influence coastal atmospheric moisture isotopic composition.
24 We identified clear seasonal patterns in the isotopic composition, with $\delta^{18}\text{O}$, δD , and d-
25 excess showing substantial variation between the southwest and northeast monsoon
26 periods. The primary moisture sources were the Arabian Sea and the Indian Ocean
27 during the southwest monsoon (May to September), characterized by small amplitude
28 fluctuations of $\delta^{18}\text{O}$ (-20.4‰ to -9.1‰). During the northeast monsoon, the northern

29 Bay of Bengal, the Indian subcontinent, and Southeast Asia were primary moisture
30 sources, resulting in large amplitude fluctuations ~~of in~~ $\delta^{18}\text{O}$ (-23.9‰ to -7.5‰) and
31 higher d-excess values (up to 25 ‰). The study also identified significant influences of
32 sea surface temperature and sea surface relative humidity on the isotopic composition
33 of water vapor. Additionally, we could use outgoing longwave radiation (OLR) to gauge
34 the intensity of convective activity. Observational periods with Lower low OLR values,
35 indicative of stronger and deeper convection, were associated with air masses that were
36 more depleted in $\delta^{18}\text{O}$ than periods with high OLR. These findings facilitate a better
37 understanding of how the monsoon and local meteorological conditions affect water
38 vapor isotope compositions in tropical region. Furthermore, the new dataset will enable
39 to improve water vapor isotopic modeling and projections of atmospheric processes in
40 coastal regions.

41 **Keywords:** Indian Summer Monsoon, Water Vapor Isotopes, Sea Surface Condition,
42 Convective Activity, Sri Lanka

43

44 **Short Summary**

45 Monitoring of atmospheric water vapor isotopes for one year at Matara, Sri Lanka,
46 yielded revealed clear seasonal variations in $\delta^{18}\text{O}$, δD , and d-excess. The results showed
47 lower amplitudes of $\delta^{18}\text{O}$ during the southwest monsoon and higher amplitudes of $\delta^{18}\text{O}$
48 and higher d-excess during the northeast monsoon. Sea surface evaporation and
49 regional convective activity significantly influenced the isotopic compositions. Overall,
50 our results facilitate an improved understanding of the impacts of the monsoon and
51 local meteorological conditions on tropical water vapor isotop~~ie compositione signals~~.

52

53 **1 Introduction**

54 The Indian Summer Monsoon (ISM), occurring from June to September, is a
55 pivotal component of the Asian climate system, serving as the primary moisture
56 transport system of moisture from the Indian Ocean to the Indian subcontinent and the
57 Tibetan Plateau (TP). Monsoonal precipitation plays a crucial role in agriculture and

58 water resource **availability**, affecting the welfare of over 1.9 billion people
59 in surrounding countries (Webster et al., 1998; Goswami et al., 2006). The Tibetan
60 climate and hydrology are profoundly influenced by the ISM, as it contributes
61 significantly to the regional water cycle by delivering substantial rainfall during the
62 summer months. This rainfall is essential for maintaining the glaciers and permafrost
63 in the TP, a key water catchment area for many of Asia's largest rivers (Bookhagen and
64 Burbank, 2010). The ISM's intensity and variability can lead to significant fluctuations
65 in water availability, affecting both agriculture and hydropower generation in the region
66 (Singh and Bengtsson, 2004; Gao et al., 2014). Furthermore, the interaction between
67 the ISM and the TP's topography creates unique climatic conditions that influence
68 weather patterns and extreme events in the region (Liu and Chen, 2000).

69 The seasonal precipitation and its origins over the TP are inextricably linked to
70 the dynamics of the ISM (Dai et al., 2021). Previous studies have provided evidence
71 that precipitation over the TP offer insights into the climatic fluctuations and distinct
72 moisture attributes associated with the ISM (Gao et al., 2013; Guo et al., 2017). The
73 summer monsoon brings significant moisture from the Indian Ocean, leading to
74 substantial rainfall over the TP primarily during the monsoon months of June-
75 September (Yao et al., 2012). This seasonal influx of moisture is critical for maintaining
76 the regional hydrological balance and supporting ecosystems. Furthermore, the ISM's
77 intensity and variability significantly influence the interannual and decadal
78 precipitation patterns over the TP, affecting the overall water availability and climatic
79 stability of the region (Kaushal et al., 2018).

80 Amidst the backdrop of global climate change, observing stable isotopes in
81 atmospheric water vapor is vital for monitoring and understanding climate shifts in low-
82 latitude areas (Rahul et al., 2016b). Such research is instrumental for providing a deeper
83 understanding of near-surface water vapor dynamics, pinpointing vapor sources and
84 transport routes, and differentiating between **different—various** contributions of
85 atmospheric water vapor to the water cycle. The stable isotopic composition of
86 precipitation (Rahul et al., 2016a; Cai et al., 2017) and water vapor (Risi et al., 2008;

87 Steen-Larsen et al., 2013b; Rahul et al., 2016b; Lekshmy et al., 2022) serves as a
88 valuable tool for identifying the origins and understanding transmission processes of
89 atmospheric water vapor. Fractionation occurs during various phase transitions, such as
90 sea surface evaporation, condensation ~~beneath-in~~ clouds, re-evaporation of raindrops
91 ~~beneath clouds~~, and diffusive exchanges between water vapor and raindrops ~~in different~~
92 ~~environments~~ (Stewart, 1975; Benetti et al., 2018; Graf et al., 2019). The occurrence of
93 fractionation unveils investigable spatiotemporal distribution patterns in the water
94 isotopic composition, encompassing water vapor and precipitation. In this context,
95 deuterium excess (d -excess = $\delta D - 8 \times \delta^{18}O$) is a useful parameter for studying kinetic
96 fractionation effects (Dansgaard, 1964). Recent studies have significantly enhanced our
97 understanding of isotopic signals in ~~convection-convective~~ regions, elucidating the
98 complex interactions between moisture processes and isotopic composition in tropical
99 deep convection ([Risi et al., 2008](#); [Blossey et al., 2010](#)). Around Barbados, during the
100 winter trade winds, vertical transport and large-scale circulation have been identified as
101 primary drivers of isotopic variability at the cloud base, acting over timescales from
102 hours to days (Bailey et al., 2023; Villiger and Aemisegger, 2024). Investigations into
103 water vapor isotopes in the West African troposphere reveal that both convection and
104 mixing highlight the important role played by large-scale atmospheric circulation
105 processes in the variations of water vapor isotopes (Diekmann et al., 2021; de Vries et
106 al., 2022). The precise mechanisms by which convective activity ~~reduces-depletes the~~
107 ~~values of stable isotopes in~~ water vapor and precipitation ~~of heavy isotopes~~ are still
108 under debate. Some researchers have emphasized the significance of condensation
109 levels (Cai and Tian, 2016; Permana et al., 2016; Thompson et al., 2017), while others
110 suggested raindrop re-evaporation and raindrop-vapor isotope exchanges during strong
111 convection as crucial factors (Galewsky et al., 2016). Additionally, unsaturated or
112 mesoscale descending airflows that transport vapor depleted in heavy isotopes to the
113 lower atmosphere also contribute to lower isotope values (Risi et al., 2008; Kurita,
114 2013). The influence of these processes varies with the intensity of convective activity.

115 Research on water vapor stable isotopes in the marine boundary layer aims to

elucidate the processes associated with evaporation in different conditions of vertical stability, wind, sea surface temperature (SST), and relative humidity with respect to the SST (RH_{SST}) isotopes as well as influencing factors (Craig and Gordon, 1965). The d-excess of evaporated water vapor is mainly impacted by kinetic fractionation and sensitive to associated with sea surface temperature (SST), the relative humidity above the sea surface (RH_{SST}, calculated relative to the saturation vapor pressure at SST), and the wind speed (rough or smooth) and the turbulence regime in the boundary layer (Merlivat and Jouzel, 1979; Benetti et al., 2015; Benetti et al., 2018). Investigations into the water vapor stable isotopic composition within the marine boundary layer have been principally focused on regions such as the North Atlantic (e.g., Greenland, Iceland, Bermuda) (Steen-Larsen et al., 2013a; Bonne et al., 2014; Benetti et al., 2018; Bonne et al., 2019), Bay of Bengal (BoB) (Lekshmy et al., 2022), and Arctic Oceans (Kurita, 2011). Several studies could confirm the existence of a negative relationship between d-excess and RH_{SST} (Uemura et al., 2008; Steen-Larsen et al., 2015), with wind speed and SST exerting a limited influence on this correlation (Benetti et al., 2015). Observations from the North Atlantic support this theory (Benetti et al., 2014). Other studies, argue that the SST does have an influence via the weak dependence of the d-excess on temperature during equilibrium fractionation based on theoretical arguments (Aemisegger and Sjolte, 2018) as well as observations in the marine boundary layer covering a large latitudinal gradient over the Atlantic and Southern Ocean (Thurnherr et al. 2020). In addition, studies found significant variations in d-excess values in vapor that originated at different moisture sources (Pfahl and Wernli, 2008; Kurita, 2011; Steen-Larsen et al., 2013b; Delattre et al., 2015). Subsequently, Benetti et al. (2015) introduced a multi-layer mixing model, which is expected to improve the accuracy of d-excess and water vapor isotope simulations. Due to the impact of kinetic fractionation on sea surface water evaporation, some studies have focused on simulating observed d-excess under the closure assumption (Merlivat and Jouzel, 1979). Others have used isotope atmospheric circulation models to assess mixing and transport processes within the marine boundary layer at different resolution (Steen-Larsen et al. 2017; Risi et al.

145 [2020; Thurnherr et al. 2021](#)[Benetti et al., 2015](#)). In addition, previous studies have used
146 single column analytical mixing models (Risi et al. 2019), as well trajectory-based box
147 models (Thurnherr and Aemisegger, 2022). Owing to the minor influence of transport-
148 induced fractionation, d-excess in the marine boundary layer is typically employed to
149 deduce moisture sources (Benetti et al., 2018).

150 Located in the northern Indian Ocean, Sri Lanka is impacted by both the southwest
151 and northeast monsoons (Fig. 1a, b) and has been identified as an important origin
152 region for monsoonal water vapor over the TP. However, only few studies have focused
153 on the Indian Ocean, and even fewer on the area around Sri Lanka. This knowledge gap
154 underscores the need to explore isotopic signals in this region and place them into their
155 appropriate context, e.g., with findings by Risi et al. (2008). For instance, more recent
156 studies on water stable isotopes in the South Indian Ocean and South Asian region have
157 uncovered connections between local processes and large-scale atmospheric circulation,
158 shedding light on sea-surface dynamics (Midhun et al., 2013; Rahul et al., 2016b;
159 Bonne et al., 2019). Unlike, in precipitation and surface water, in atmospheric water
160 vapor stable isotopes can be monitored continuously regardless of season, weather, or
161 location (Angert et al., 2008). This potentially full temporal and spatial coverage allows
162 for a more comprehensive and continuous monitoring of atmospheric water vapor
163 dynamics and transport, which should in turn facilitate a deeper understanding of
164 isotope transformation processes within the water cycle. Therefore, investigating the
165 dynamics of near-surface atmospheric water vapor stable isotopes at coastal stations is
166 not only pivotal for identifying monsoonal water vapor source regions but will facilitate
167 a better understanding of precipitation processes over the Indian Ocean. Oceanic
168 evaporation represents the first of many phase transitions that occur during the global
169 water cycle. The primary objective of researching water vapor stable isotopes is to
170 comprehend the processes and controlling factors of water isotopic variations.

171 In this study, we present the results from continuous observations of near-surface
172 atmospheric water vapor stable isotopes in Matara, Sri Lanka, collected from March 1,
173 2020, to February 28, 2021. We analyze the observational data to gain a better

174 understanding of the variations in moisture sources and main transmission processes in
175 tropical coastal regions. Furthermore, we explore how sea surface processes, convective
176 activity, and local meteorological factors affect near-surface atmospheric water vapor
177 stable isotopes at a coastal station, across daily, monthly, and seasonal (monsoonal) time
178 scales. Section 2 gives an overview of the study site and presents the meteorological
179 and water vapor observations, calibration protocols, and analysis methods. In Section
180 3, we illustrate the variability of isotopic and meteorological parameters, analyze
181 moisture sources, assess the impact of sea surface processes on water vapor isotopes,
182 and explore the relationship between water vapor isotopes, convective activity, and
183 local meteorological observations.

184

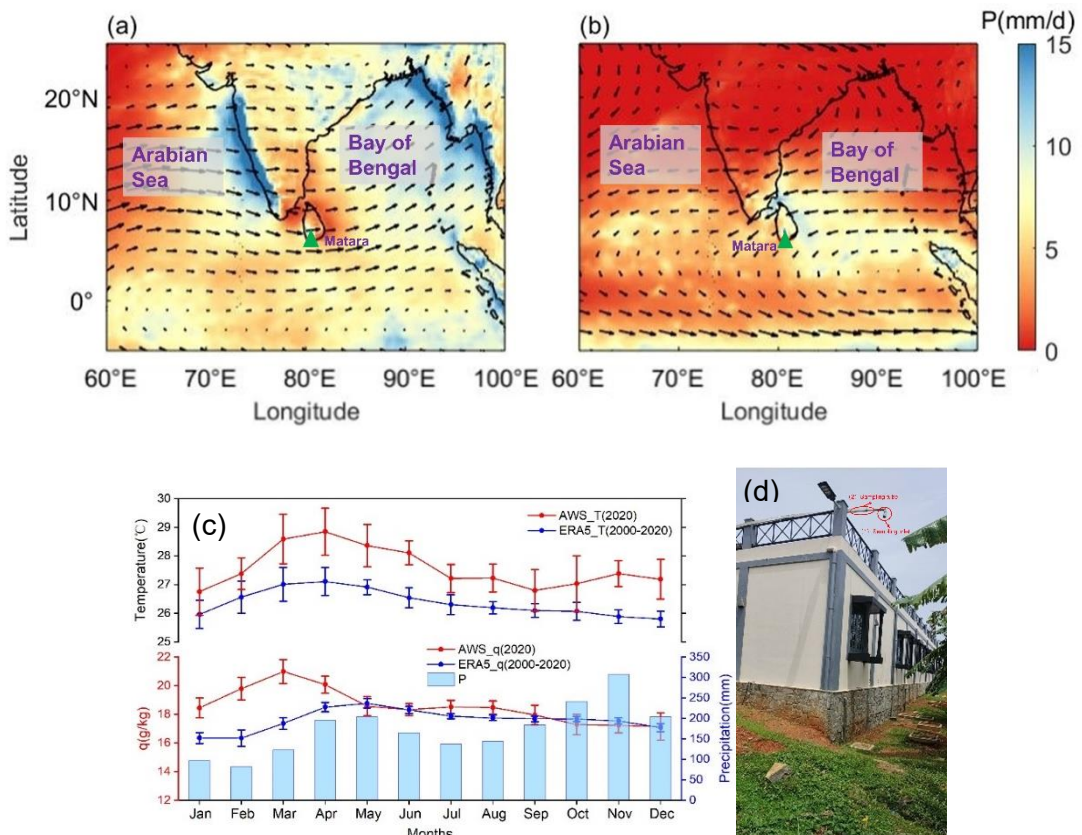
185 **2 Study Site, Data, and Methods**

186 **2.1 Study Site and Meteorological Data**

187 Sri Lanka (located between approximately 6°N to 10°N and 79° to 82°E) is the
188 southernmost country on the Indian subcontinent and a key region for identifying the
189 moisture source of the south Asian summer monsoon (Ravisankar et al., 2015).
190 Featuring a tropical climate, Sri Lanka experiences four distinct monsoon seasons
191 annually: the northeast monsoon from December to February, the first inter-monsoon
192 from March to April, the southwest monsoon from May to September, and the second
193 inter-monsoon from October to November (Malmgren et al., 2003; Jayasena et al.,
194 2008). For the analyses, we combined the first and second inter-monsoon periods into
195 a single “non-monsoon period”. Most of the precipitation in Sri Lanka comes from the
196 southwest and northeast monsoon systems, accounting for over 78% of the total annual
197 precipitation (Fig. 1c). Precipitation formation in Sri Lanka primarily relies on
198 organized convection associated with the Intertropical Convergence Zone (ITCZ) and
199 low-pressure systems (Gadgil, 2003), while the associated moisture primarily originates
200 in the Indian Ocean and BoB (Bandara et al., 2022). The southwest monsoon transports
201 moisture from the Indian Ocean to southwestern Sri Lanka (Fig. 1a) where it leads to
202 increased rainfall (Bavadekar and Mooley, 1981). In contrast, the northeast monsoon

203 carries water vapor from the BoB to northern and northeastern of Sri Lanka (Fig. 1b)
 204 (Dhar and Rakhecha, 1983; Wang, 2006).

205 An automated weather station (AWS) was installed at the University of Ruhuna,
 206 Matara (located at 5.94°N, 80.57°E) on the southern coast of Sri Lanka (Fig. 1d). It
 207 collected real-time meteorological observations, including air temperature,
 208 precipitation, relative humidity, air pressure, wind speed, and wind direction, from
 209 March 1, 2020, to February 28, 2021.



210
 211 **Figure 1: Mean wind vectors (arrows) at 850 hPa during the (a) 2020 southwest monsoon and**
(b) 2020/2021 northeast monsoon seasons, along with mean precipitation (P, base colors) from
ERA5 averaged for the same period. (c) Monthly mean temperature and specific humidity (q)
obtained from the automated weather station at Matara (January and February are from 2021
while March – December from 2020), with monthly average temperature, specific humidity,
and precipitation from ERA5 (averaged for the years 2000-2020) plotted for comparison. (d)
Photograph of the roof-mounted weather station at the University of Ruhuna, Sri Lanka.

212 In this study, we used hourly data of 2m air temperature, 2m dew temperature, air

220 pressure, precipitation, SST, atmospheric boundary layer height (BLH), wind speed,
 221 wind direction, and outgoing longwave radiation (OLR), obtained from ERA5 for years
 222 2000 to 2021, with a spatial resolution of $0.25^\circ \times 0.25^\circ$ and a temporal resolution of one
 223 hour. Meteorological data are compared with water vapor isotopic data measured during
 224 the same period. Based on the European Centre for Medium-Range Weather Forecasts
 225 (ECMWF, <https://cds.climate.copernicus.eu/eu/>) reanalysis dataset (ERA5), the annual
 226 average precipitation and air temperature for the period from 2000 to 2020 is 2085 mm
 227 and 27.6°C , respectively (Fig. 1c) (Hersbach et al., 2020). Studies have shown that
 228 ERA5 data provide good representations of the Matara equatorial climate and can be
 229 used in lieu of missing observational data (Fig. S3) (Bandara et al., 2022). Due to
 230 weather conditions and instrument trouble, specific humidity measured by the isotopic
 231 measurement instrument and computed by the AWS are missing from March, 2020 to
 232 April, 2020. Therefore, we chose to present both variables obtained from ERA5 as they
 233 complement each other, providing a clearer picture of humidity changes at Matara
 234 station.

235 For the atmosphere above open sea regions, RH_{SST} is obtained using (Bonne et al.,
 236 2019):

$$\text{RH}_{\text{SST}} = \text{RH}_{2\text{m air}} \times \frac{q_{\text{sat}}(T_{2\text{m air}})}{q_{\text{sat}}(\text{SST})} \quad (6)$$

237 where $\text{RH}_{2\text{m air}}$ is the relative humidity 2m above the ocean surface, $q_{\text{sat}}(T_{2\text{m air}})$ is
 238 the specific humidity at a saturated condition for a given 2m air temperature, and
 239 $q_{\text{sat}}(\text{SST})$ is calculated for seawater with a salinity of 35 practical salinity units (PSU)
 240 (Curry and Webster, 1999).

241 The formulas to calculate air saturation specific humidity $q_{\text{sat}}(T_{2\text{m air}})$ and sea
 242 surface saturation specific humidity $q_{\text{sat}}(\text{SST})$ with a salinity of 35 PSU are:

$$q_{\text{sat}}(T_{2\text{m air}}) = \frac{0.622 \times E}{P} \quad (7)$$

$$q_{\text{sat}}(\text{SST}) = 0.98 \times q_s \quad (8)$$

243 q_s represents specific humidity with a salinity of 35 PSU and is calculated in the same
244 way as $q_{sat}(T_{2m\ air})$. E is the saturated water vapor pressure, obtained from the
245 improved Goff-Gratch formula (Goff and Gratch, 1946). P is atmospheric pressure. We
246 take the sea surface pressure as the atmospheric pressure to participate in the above
247 calculation (Eq. 7).

248 **2.2 In-situ Observations of Atmospheric Water Vapor Isotopic
249 Composition**

250 Near-surface atmospheric water vapor isotope measurements at Matara were
251 collected using a sampling frequency of 1Hz with the instrument located approximately
252 5m from the AWS. We used a Water Vapor Isotope Analyzer (Los Gatos Research (LGR)
253 Inc.) in conjunction with an LGR Water Vapor Isotope Standard Source (WVISS) model.
254 The LGR instrument employs a mirrored sampling chamber in which the laser traverses
255 the sample volume thousands of times, effectively amplifying the water vapor
256 absorption signal which facilitates the detection of low concentrations of D and ^{18}O
257 (Liu et al., 2015). Compared to traditional methods, this spectroscopic technique offers
258 three advantages: (i) it is compact and portable, enabling real-time field monitoring; (ii)
259 it can simultaneously measure $\delta^{18}\text{O}$ and δD ; and (iii) it has lower measurement costs
260 and requires less operator expertise.

261 The instrumental setup was situated approximately 100 m from the sea shore (5.94°
262 N, 80.57° E, 10 meters), and consisted of four primary components: (1) A sampling
263 inlet, positioned approximately 5 m above the ground (Fig. 1d), equipped with a
264 stainless-steel mesh to prevent interference from insects and facing downward to avoid
265 direct impacts from rain. (2) A 1/4-inch outer diameter stainless steel sampling tube,
266 insulated with heating tape and a 2-cm thick pipe for thermal insulation. (3) The
267 calibration unit to generate a constant flow of water vapor with known isotopic
268 composition and at different humidity levels. (4) A water vapor isotope analyzer,
269 delivering a measurement precision for $\delta^{18}\text{O}$ and δD of $0.25\text{\textperthousand}$ and $0.5\text{\textperthousand}$, respectively
270 (a concentration of 2500 ppmv). This setup has been designed to minimize external

271 influences and maintain the integrity of the sampled water vapor.

272 The spatial proximity between the water vapor analyzer and AWS ensures a high
273 level of synchronicity between the isotope and meteorological measurements. We
274 define wind directions from 60° to 330°N as oceanic, while those from 330° to 60°N as
275 terrestrial winds (Fig. 1a, b).

276 Atmospheric water vapor stable isotopes are expressed using the δ notation (in per
277 mil, ‰), using the following equations:

$$R_{^{18}O} = \frac{^{18}O}{^{16}O} \quad (9)$$

$$R_D = \frac{D}{^1H} \quad (10)$$

$$\delta_{sample} = \left(\frac{R_{sample}}{R_{VSMOW}} - 1 \right) \times 1000\% \quad (11)$$

278 Here, δ_{sample} represents either $\delta^{18}O$ or δD (^{18}O or D isotope ratio) relative to Vienna
279 Standard Mean Ocean Water (VSMOW). R_{sample} and R_{VSMOW} are the ^{18}O or D and
280 VSMOW isotope ratios, respectively.

281 2.3 Calibration Protocol

282 In this study, we adhere to the calibration protocol proposed by Steen-Larsen et al.
283 (2013b). Briefly, the instrument calibration and data processing consist of three major
284 steps: (1) humidity-isotope response calibration, (2) VSMOW - Standard Light
285 Antarctic Precipitation (VSMOW-SLAP) calibration, and (3) drift correction (see Text
286 S1 in the Supporting Information).

287 The water vapor concentration can influence the measured water vapor isotopic
288 composition, known as concentration- or humidity-isotope dependency
289 characterization. By adding a constant stream of water vapor with known isotopic
290 composition at different humidity levels, we can establish the humidity-isotope
291 response function (Sturm and Knohl, 2010; Aemisegger et al., 2012). As this function
292 can vary over time, its calibration was repeated monthly, using two standard samples of
293 known isotopic compositions measured at humidity levels ranging from 16,000 to
294 38,000 ppmv at intervals of 1000 ppmv. Each level was measured for at least 25 minutes

295 using the LGR WVISS. Our results are referenced to a humidity level of 20,000 ppmv.
296 We compared our measurements to the international VSMOW-SLAP scale, assuming a
297 linear drift between calibration points.

298 To compensate for instrumental drift, we measured the water vapor from a drift-
299 standard bottle for 25 minutes after each 12 hours performed an ambient air
300 measurement. Furthermore, we tested for instrument drift as part of the routine
301 instrument maintenance, assuming a linear drift between each drift-standard
302 measurement. Laboratory analyses of liquid isotopes have confirmed the stability of its
303 isotopic composition over time.

304 **2.4 Rayleigh Distillation Model and MBL-Mixing Model**

305 The Rayleigh distillation model is employed to quantify isotopic variations during
306 phase changes (Dansgaard, 1964), by which the residual air mass becomes drier with a
307 depletion in heavy isotopes following moist adiabatic vertical ascent (Gat, 1996):

$$308 R_r = R_0 f^{\alpha_v^l(T) - 1} \quad (12)$$

309 Here, R_r and R_0 represent the isotopic ratio of residual vapor and initial vapor,
310 respectively. $\alpha_v^l(T)$ denotes the equilibrium fractionation factor, and f is the fraction
311 of residual water vapor.

312 By integrating the definition of isotope ratios as given in Equation (11), the
313 Rayleigh distillation model can be expressed in terms of isotopic content as follows:

$$\delta_r = (\delta_0 + 1) f^{\alpha_v^l(T) - 1} - 1 \quad (13)$$

314 where δ_r and δ_0 are the isotope ratios relative to VSMOW in residual and initial vapor,
315 respectively.

316 We employ the mixing model to examine the isotopic characteristics after the
317 mixing of two air masses (Galewsky and Hurley, 2010):

$$R_{\text{mix}} = \frac{f[\text{HDO}]_1 + (1 - f) \times [\text{HDO}]_2}{f[\text{H}_2\text{O}]_1 + (1 - f) \times [\text{H}_2\text{O}]_2} \quad (14)$$

$$R_{\text{mix}} = \frac{f[\text{H}_2^{18}\text{O}]_1 + (1 - f) \times [\text{H}_2^{18}\text{O}]_2}{f[\text{H}_2\text{O}]_1 + (1 - f) \times [\text{H}_2\text{O}]_2} \quad (15)$$

318 where R_{mix} represents the isotopic ratio of the mixed air mass, while $[\text{HDO}]$, $[\text{H}_2\text{O}]$, and

318 $[\text{H}_2^{18}\text{O}]$ denote isotopic water vapor volume mixing ratios, and f is the mixing fraction.
319 The isotopic ratio and isotopic δ in the Eq. 14 and Eq. 15 have been calibrated by
320 VSMOW.

321 We use water vapor isotopes to characterize the mixing processes in the marine
322 boundary layer (MBL) (Benetti et al., 2018), using the following equation (Craig and
323 Gordon, 1965):

$$1 + \delta_e = \frac{1}{\alpha_k} \times \frac{\alpha_v^l \times (1 + \delta_{OC}) - RH_{SST} \times (1 + \delta_{MBL})}{1 - RH_{SST}} \quad (16)$$

324 where α_v^l represents the equilibrium fractionation factor between vapor and liquid, and
325 α_k is the kinetic fractionation factor. δ_{OC} denotes the isotopic composition of the ocean
326 surface. We utilize α_v^l from Majoube (1971a, b) and α_k for the smooth regime ($\alpha_k^{18}\text{O} =$
327 1.006 and $\alpha_k D = 1.0053$) (Merlivat and Jouzel, 1979).

328 **2.5 Concentration-WeightedQualitative Trajectory-based and** 329 **Moisture Source DiagnosesAnalysis**

330 To delineate water vapor transport paths and pinpoint moisture sources, we
331 employed the Hybrid Single-Particle Lagrangian Integrated Trajectory (HYSPLIT)
332 model from the US National Oceanic and Atmospheric Administration (NOAA) to
333 compute backward trajectories of air masses arriving at Matara station during the
334 southwest and northeast monsoons. The Global Data Assimilation System (GDAS) with
335 $1^\circ \times 1^\circ$ and 3-hour spatial and temporal resolutions provided the background
336 meteorological data from May 2020 to September 2020 and December 2020 to
337 February 2021 (<ftp://arlftp.arlhq.noaa.gov/archives/gdas1/>). The HYSPLIT model uses
338 GDAS reanalysis data, which contains 37 (vertical) pressure levels and a $1^\circ \times 1^\circ$
339 horizontal resolution. Atmospheric water vapor primarily resides at altitudes below 2
340 km (Wallace and Hobbs, 2006). In this study, particles were released four times daily
341 (at 00:00, 06:00, 12:00, and 18:00 UTC) at 20 different locations within a rectangular
342 area extending 0.2° in each direction (north, south, east, and west) from Matara station
343 and at four heights above the ground (50 m, 500 m, 1200 m, and 2000 m). Each

344 trajectory was back-traced for 168 h, recording data at 1-h intervals. The HYSPLIT
345 model outputs latitude, longitude, elevation, pressure, temperature, precipitation,
346 relative humidity, and specific humidity. Backward trajectory clustering analysis was
347 conducted, using the corresponding meteorological data. We averaged the trajectories
348 of four times per day to obtain a daily mean trajectory, combined with water vapor
349 stable isotope values on precipitation days. These daily mean trajectories were clustered
350 by moisture source using K-means clustering. By analyzing the variations in latitude,
351 elevation, and specific humidity along the trajectories, the influence of different
352 moisture sources on local vapor content and isotopic composition was evaluated.

353 These analyses yielded concentration-weighted trajectory (CWT) fields
354 (resolution of $0.5^\circ \times 0.5^\circ$) (Hsu et al., 2003) using the in-situ daily average $\delta^{18}\text{O}$ and d-
355 excess, which in turn facilitated the identification of potential moisture sources and an
356 assessment of the potential influence of recirculation on d-excess in water vapor
357 (Salamalikis et al., 2015; Bedaso and Wu, 2020; Xu et al., 2022). CWT (C_{ij}) was
358 calculated as:

$$C_{ij} = \frac{\sum_{k=1}^K C_k \tau_{ijk}}{\sum_{k=1}^K \tau_{ijk}} \quad (17)$$

359 where (i, j) denote grid coordinates, k the trajectory index, K the total number of
360 trajectories analyzed, C_k the concentration (here $\delta^{18}\text{O}$ and d-excess) at the end of the
361 trajectory k , and τ_{ijk} the residence time of trajectory k in grid cell (i, j) . We substituted
362 the residence time by the number of trajectory endpoints in each grid cell (i, j) .

363

364 **3 Results**

365 **3.1 Seasonal Variability of Water Vapor Stable Isotope**

366 366 During a year-long observational period (1 March 2020 to 28 February 2021), the
367 367 seasonal and synoptic variations observed in water vapor isotopes ($\delta^{18}\text{O}$, δD , and d-
368 368 excess) and key meteorological parameters (temperature, relative humidity,
369 369 atmospheric pressure, specific humidity, and SST) are explored (Fig. 2), aiming to
370 370 provide insights into the interactions between atmospheric and oceanic conditions at

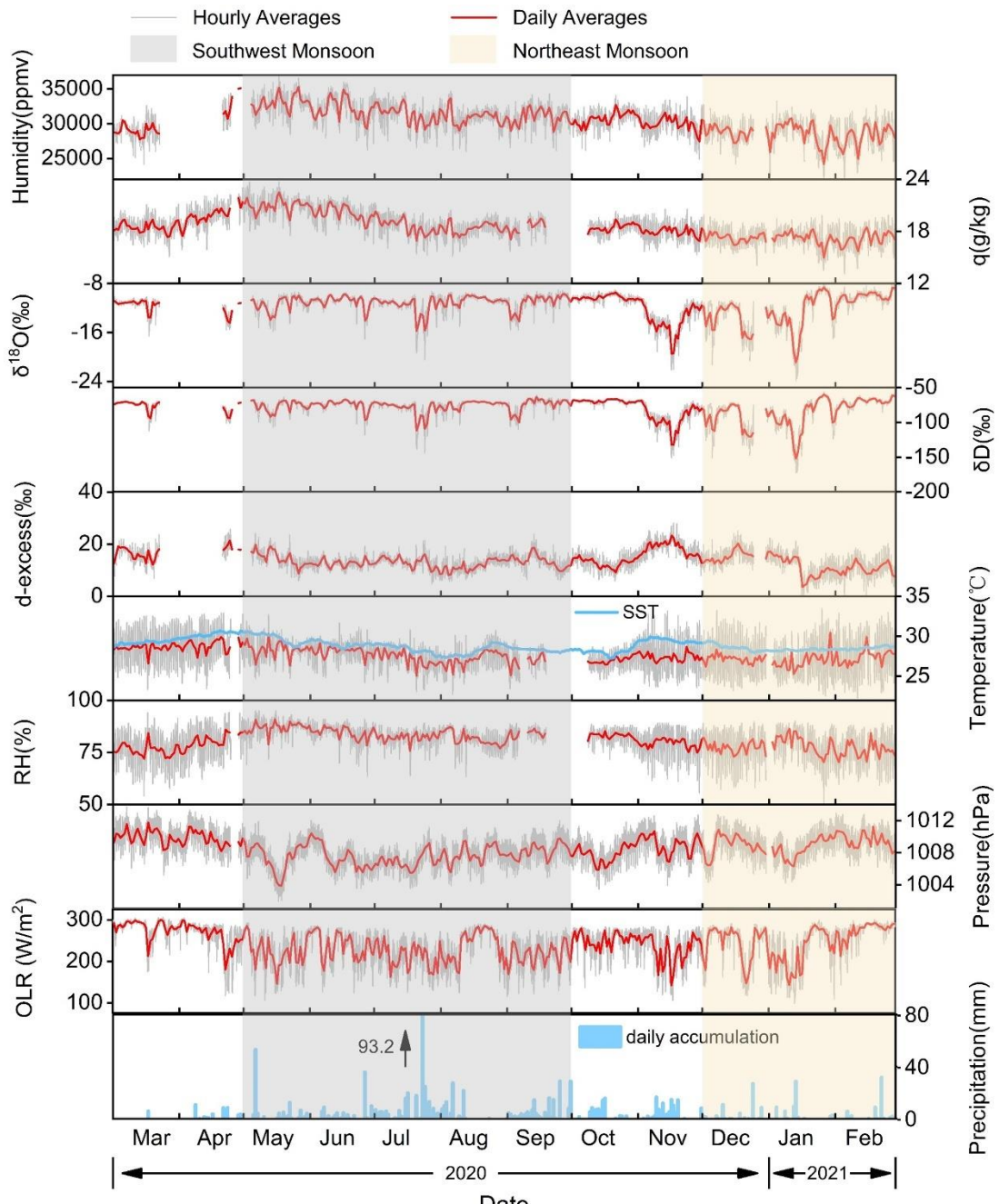
371 Matara. The tropical setting at Matara leads to relatively modest temperature
372 fluctuations, with Fig. 2 shows the hourly and daily averages of water vapor isotopes
373 ($\delta^{18}\text{O}$, δD , and d excess) alongside temperature, relative humidity, atmospheric
374 pressure, specific humidity, and SST at Matara station.

375 We demonstrated the monthly variations of the average relative humidity, specific
376 humidity, monthly precipitation, and water vapor isotopic composition ($\delta^{18}\text{O}$, δD , and
377 d excess) (Fig. S4 and Table 1). The 12-month average temperature and relative
378 humidity are at 27.6°C , dipping to 22.3°C and reaching 33.5°C at extremes, and 80.7%,
379 respectively (Table 1). Temperature variations maintain consistent The amplitude of
380 temperatures between monsoon and non-monsoon periods remains at around 10°C
381 between monsoon and non-monsoon periods. Specific humidity ranging from 16 g/kg
382 to 21 g/kg and shows marked oscillations during the southwest and northeast monsoons,
383 with amplitudes of approximately 1.3 g/kg and 2.3 g/kg, respectively. Relative humidity
384 also shows clear seasonal pattern, peaking at 95% in May (southwest monsoon) and
385 falling to 49.2% in January (northeast monsoon). Monthly trends (Fig. S4 and Table 1)
386 reveals a steady decrease in both air temperature and specific humidity from May to
387 September, culminating in their lowest values (26.9°C and 18.5 g/kg, respectively).
388 Recorded minimum and maximum temperatures are 22.3°C and 33.5°C , respectively.
389 Specifically, comparing monthly variations in air temperature and specific humidity
390 (Fig. S4), both parameters gradually decrease from relatively high values in May to
391 their respective minima of 26.9°C and 18.5 g/kg (monthly averages) in September.
392 Monthly average air temperature and specific humidity show continuous increases from
393 January to 28.4°C and 21 g/kg in May. Also, mean relative humidity peaks in May at
394 95%, with lower values observed during the northeast monsoon and the early first non-
395 monsoon (December to April), reaching a minimum of 49.2% in January. From late
396 May, specific humidity gradually declines, stabilizing after mid July until October with
397 levels ranging from 16 g/kg to 20 g/kg. Significant oscillations occur during the
398 southwest and northeast monsoons, with amplitudes of approximately 1.3 g/kg and 2.3
399 g/kg, respectively. During the southwest monsoon, temperature~~s~~, and specific humidity

400 peak in May (monthly averages of $28.4 \pm 1.4^{\circ}\text{C}$ and $21.0 \pm 1.1 \text{ g/kg}$) reflect the influx
401 of warm, moist air from the Indian Ocean. In contrast, February marks stands out as the
402 coldest and driest period (specific humidity) month (monthly averages of $27.4 \pm 2.6^{\circ}\text{C}$
403 and $17.1 \pm 1.3 \text{ g/kg}$) corresponding during to the northeast monsoon (Fig. S4). The
404 seasonal temperature variations Among them, exhibit modest amplitudes (Fig. 2),
405 attributed to the tropical climate at Matara station. Conversely, relative humidity
406 displays higher amplitude seasonal than synoptic variations. Furthermore, daily average
407 SSTs consistently exceed the daily average 2m air temperatures recorded by the AWS,
408 indicating the ocean's significant role in modulating near-surface atmospheric
409 conditions (Fig. 2). (Fig. 2).

410 Yearly averages for water vapor isotopic values are $-11.6\text{\textperthousand}$ for $\delta^{18}\text{O}$, $-79.5\text{\textperthousand}$ for
411 δD , and $13.3\text{\textperthousand}$ for d-excess, respectively. Isotopic composition ranges from $-23.9\text{\textperthousand}$ to
412 $-7.5\text{\textperthousand}$ for $\delta^{18}\text{O}$, $-173.2\text{\textperthousand}$ to $-53.4\text{\textperthousand}$ for δD , and $-1.2\text{\textperthousand}$ to $28.1\text{\textperthousand}$ for d-excess (Table
413 1). Monthly averages of water vapor isotopes ($\delta^{18}\text{O}$ and d-excess) exhibit stability from
414 March to October, followed by sudden decreases. $\delta^{18}\text{O}$ and δD show distinct seasonal
415 variations, with higher values during the southwest monsoon and lower values during
416 the northeast monsoon (Table 1). Therefore, the subsequent analysis will concentrate
417 on the variations in $\delta^{18}\text{O}$. During the southwest monsoon, the northeast monsoon, and
418 the non-monsoon periods, the average values of $\delta^{18}\text{O}$ are $-11.1\text{\textperthousand}$, $-12.2\text{\textperthousand}$, and $-11.9\text{\textperthousand}$,
419 respectively. Extreme values of $\delta^{18}\text{O}$ are observed during the northeast monsoon, with
420 a maximum of $-7.5\text{\textperthousand}$ and a minimum of $-23.9\text{\textperthousand}$. Conversely, d-excess exhibits a
421 reverse pattern to $\delta^{18}\text{O}$ on both seasonal and monthly scales, characterized by lower
422 values during the southwest monsoon and higher values during the non-monsoon period.
423 Furthermore, during the northeast monsoon, the southwest monsoon, and the non-
424 monsoon periods, the average values of d-excess are $12.4\text{\textperthousand}$, $13\text{\textperthousand}$, and $14.7\text{\textperthousand}$,
425 respectively. The d-excess maximum occurs in November at $28.1\text{\textperthousand}$ (monthly average
426 of $15.2 \pm 4.3\text{\textperthousand}$), while the minimum of $-1.2\text{\textperthousand}$ was recorded in January (monthly
427 average of $11.3 \pm 4.5\text{\textperthousand}$). The high values of d-excess are related to moisture recycling.
428 Low specific humidity corresponds to depleted $\delta^{18}\text{O}$ and elevated d-excess, indicating

429 a strong depletion during the long-distance transport from the source regions to the
 430 observation station. Coastal stations such as Bangalore, Ponmudi, and Wayanad also
 431 show similar water vapor isotopic depletion in autumn and winter, reflecting the
 432 observations made at Matara (Table 2).



433

434 **Figure 2: Near-surface observations at Matara station of water vapor isotopes ($\delta^{18}\text{O}$, δD , and**
 435 **d-excess) and meteorological parameters (humidity, specific humidity (q), temperature,**
 436 **relative humidity (RH), pressure, outgoing longwave radiation (OLR, obtained from NCEP),**

437 **and precipitation) from March 1, 2020, to February 28, 2021. Local sea surface temperature**
438 **at Matara (SST, obtained from ERA5) is plotted in blue.**

439 For $\delta^{18}\text{O}$, δD , and d-excess, synoptic variations were recorded (Fig. 2). Abrupt
440 changes occurred in late July 2020 and from November 2020 to January 2021,
441 associated with synoptic events. Cumulative precipitation in July 2020 reached 451.8
442 mm, with a notable rainfall event in late July recording daily rainfall of 93.2 mm.
443 Isotopic $\delta^{18}\text{O}$ values show a sharp depletion from $-10.4\text{\textperthousand}$ to $-20.4\text{\textperthousand}$ within 20 h of
444 isolated rainfall events, lasting for 6 days. Over the 75-day period spanning from late
445 southwest monsoon to mid-northeast monsoon, significant fluctuations can be seen in
446 isotopic $\delta^{18}\text{O}$ between $-22\text{\textperthousand}$ and $-11\text{\textperthousand}$. During the southwest monsoon from July 12
447 to August 7, $\delta^{18}\text{O}$ values varied from $-20.4\text{\textperthousand}$ to $-9.2\text{\textperthousand}$, and δD values ranged from -
448 $143.5\text{\textperthousand}$ to $-68.6\text{\textperthousand}$. This finding is consistent with water vapor isotopic $\delta^{18}\text{O}$ ($-14.1\text{\textperthousand}$
449 to $-9.8\text{\textperthousand}$) and δD ($-97.2\text{\textperthousand}$ to $69.1\text{\textperthousand}$) values measured from July 12 to August 7, 2012,
450 near the Bay of Bengal, although the local minimum at Matara station is below the
451 minimum in the Bay of Bengal (Midhun et al., 2013).

452 **Table 1: Summary of hourly-averaged data collected at Matara station from March 1, 2020,**
 453 **to February 28, 2021.** Averages are shown in **bold**. N indicates the number of observations of
 454 $\delta^{18}\text{O}$, δD , d-excess, temperature (T), relative humidity (RH), specific humidity (q), and
 455 atmospheric boundary layer height (BLH). Yearly maxima and minima for each parameter
 456 are highlighted using **bold italics**.

Season		$\delta^{18}\text{O}$	δD	d-excess	T	RH	q	BLH
		(‰)	(‰)	(‰)	(°C)	(%)	(g/kg)	(m)
Non- monsoon	mean	-11.9	-80.6	14.7	28.0	79.4	18.6	630.1
	SD	2.2	16.6	3.8	2.2	7.3	1.3	179.1
	Max.	-9.0	-65.3	28.1	33.2	94.2	23.0	1178.8
	Min.	-22.1	-151.1	5.1	23.3	54.2	15.1	84.4
	N	1851	1851	1851	2617	2617	2617	2928
Southwest monsoon	mean	-11.1	-75.7	13.0	27.6	83.8	19.4	741.4
	SD	1.3	9.6	2.8	1.5	4.5	1.5	149.0
	Max.	-9.1	-60.8	24.1	32.7	95.0	23.7	1564.4
	Min.	-20.4	-143.5	4.5	22.7	63.4	15.1	259.0
	N	3314	3314	3314	3192	3197	3192	3672
Northeast monsoon	mean	-12.2	-85.1	12.4	27.1	77.4	17.2	516.4
	SD	3.0	22.0	4.29	2.4	7.8	1.2	139.4
	Max.	-7.5	-53.4	25.0	33.5	90.0	19.9	1125.7
	Min.	-23.9	-173.2	-1.2	22.3	49.2	13.1	182.0
	N	1885	1885	1885	1993	1993	1993	2160
All	mean	-11.6	-79.5	13.3	27.6	80.7	18.6	648.7
	SD	2.2	16.1	3.6	2.0	7.0	2.1	181.3
	Max.	-7.5	-53.4	28.1	33.5	95.0	23.7	1564.4
	Min.	-23.9	-173.2	-1.2	22.3	49.2	13.1	84.4
	N	7050	7050	7050	7802	7807	7807	8760

457

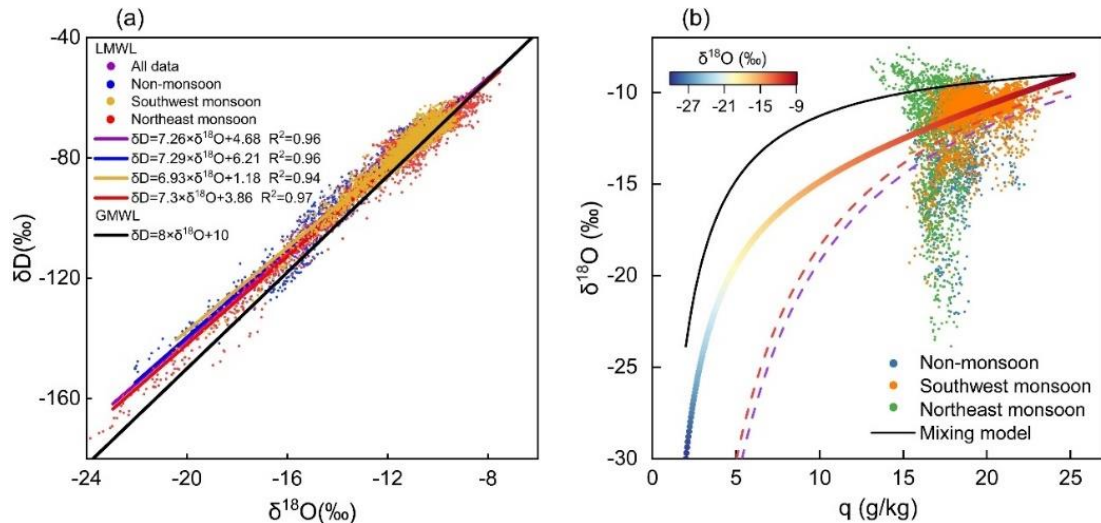
458 The atmospheric water vapor line serves as an indicator of the humidity conditions
459 at the vapor source and the fractionation processes along the transport path. The slope
460 reflects the extent of vapor kinetic fractionation, while the intercept indicates the
461 humidity levels at the vapor source. Comparing the Local Meteoric Water Line (LMWL)
462 for $\delta^{18}\text{O}$ and δD with the Global Meteoric Water Line (GMWL) we obtain a slope of <
463 8 during both monsoon periods (Fig. 3a). Seasonal variations are also visible in $\delta^{18}\text{O}$
464 and δD distribution patterns. Daily averages of water vapor isotopic $\delta^{18}\text{O}$ and δD
465 demonstrate a strong correlation ($r = 0.96$, slope = 7.26) with a lower intercept at 4.68.
466 The LMWL slope and intercept vary significantly between monsoon and non-monsoon
467 seasons, peaking in the northeast monsoon with values of 7.3 and 3.86, and nadir in the
468 southwest monsoon with 6.93 and 1.18, respectively. This suggests increased humidity
469 over sea surface vapor sources from the northeast to southwest monsoon, attributed to
470 heightened evaporation and reduced dynamic fractionation effects. During the northeast
471 monsoon, LMWL slope and intercept are higher compared to other periods, indicating
472 significant moisture recirculation.

473 **Table 2: Summary of observed water vapor isotope concentrations at various stations in India**
 474 **and the Bay of Bengal.**

Country or region	Station or location	Latitude (N°)	Longitude (E°)	Date	$\delta^{18}\text{O}$ (‰)	δD (‰)	d-excess (‰)	References
India	Bangalore	13.01	77.55	Jun 1, 2012, to	-23.8	-178.3	-4.5 to	
				Sep 30, 2012	to -9.0	to -58.6	32.7	
				Oct 1, 2012, to	-22.7	-177.1	-9.5 to	(Rahul et al., 2016b)
				Feb 28, 2013	to -10.2	to -73.7	41.4	
	Kolkata	22.56	88.41	May 3, 2019, to	-16.9	-128.3	-7.1 to	
				Oct 25, 2019	to -10.0	to -72.8	25.4	(Bhattacharya et al., 2021)
	Roorkee	29.87	77.88	Feb 1, 2007, to	-17.0		32.0 to	
				May 31, 2007	to -3.0		70.0	
				Jun 1, 2007, to	-32.0	none	40.0 to	
				Sep 30, 2007	to -6.0		87.0	(Saranya et al., 2018)
Bay of Bengal	Ponmudi	8.76	77.12	Oct 1, 2007, to	-30.0		30.0 to	
				Dec 31, 2007	to -7.0		60.0	
	Wayanad	11.51	76.02	Apr 1, 2012, to	-24.1	-170.0	6.3 to	
				Nov 30, 2012	to -8.6	to -51.0	26.5	(Lekshmy et al., 2018)
	Ahmedabad	23.03	72.56	Apr 1, 2007, to	-20.5	-139.1	13.3 to	
				Apr 1, 2008	to -7.9	to -50.0	31.2	
	Chhotashigri	32.58	77.58	Apr 1, 2007, to	-19.2	-128.1	6.9 to	
				Apr 1, 2008	to -8.9	to -59.8	40.4	(Srivastava et al., 2015)
	6m	32.58	77.58	Apr 1, 2007, to	-19.4	-101.5	28.0 to	
				Apr 1, 2008	to -10.3	to -29.2	62.0	(Ranjan et al., 2021)
Bay of Bengal	25m	25m	none	Jul 1, 2012, to	-13.6	-94.0 to	5.7 to	
				Aug 1, 2012	to -10.0	-68.3	16.4	(Midhun et al., 2013)
	25m	25m	none	Nov 15, 2013, to	-14.1	-97.2 to	6.9 to	
				Dec 1, 2013	to -9.8	-69.1	19.4	

475 We found a significant negative relationship between d-excess and $\delta^{18}\text{O}$, with a
 476 rate of change for d-excess with $\delta^{18}\text{O}$ is $-0.68 \text{‰}/\text{‰}$ ($r = -0.55$) (Fig. S5a). This below
 477 the $-0.05 \text{‰}/\text{‰}$ recorded at Bangalore station (Rahul et al., 2016b). Seasonally, the
 478 correlation between both variables have weaken during the southwest, northeast, and
 479 non-monsoon periods, with respective rates of change of $-0.94 \text{‰}/\text{‰}$ ($r = -0.49$), -

480 0.69 ‰/‰ ($r = -0.54$), and -0.65 ‰/‰ ($r = -0.44$). Similar patterns are detected for
 481 temperature–d-excess and specific humidity–d-excess correlations, showing gradual
 482 increases in the slopes and intercepts of the water vapor line. Moreover, the
 483 concentrated distribution of vapor values during the southwest monsoon and the highly
 484 scattered distribution during the northeast monsoon are indicative of the corresponding
 485 seasonal distributions of the water vapor line.



486
 487 **Figure 3: (a) Co-variation of water vapor isotopic composition and meteorological parameters**
 488 **during different monsoon and non-monsoon periods between March 1, 2020 and February 28,**
 489 **2021. The lines represent linear least-squares regressions (LMWL and GMWL) of δD (‰) as**
 490 **a function of $\delta^{18}\text{O}$ (‰). (b) Scatter plot of observed hourly water vapor isotopic $\delta^{18}\text{O}$ vs.**
 491 **specific humidity (q). The dashed red and blue curves represent the Rayleigh distillation line**
 492 **during the southwest and northeast monsoon. The solid black curve represents the mixing line.**
 493 **The colored curve represents the MBL-mixing line.**

494 Plots of $q-\delta^{18}\text{O}$, the theoretical Rayleigh distillation curve, the mixing-line, and
 495 MBL-mixing curve, were used to assess mixing conditions during the study period (Fig.
 496 3b). During the southwest monsoon, most measurements are clustered between the
 497 Rayleigh and mixing curve, indicating isotopic variability dominated by effects of
 498 precipitation and moisture mixing process. Limited water vapor measurements are
 499 scattered below the Rayleigh fractionation line, implying a discernible impact of
 500 raindrop re-evaporation. Similarly, during the non-monsoon period, most
 501 measurements lie between the Rayleigh and mixing curves, with only a few located

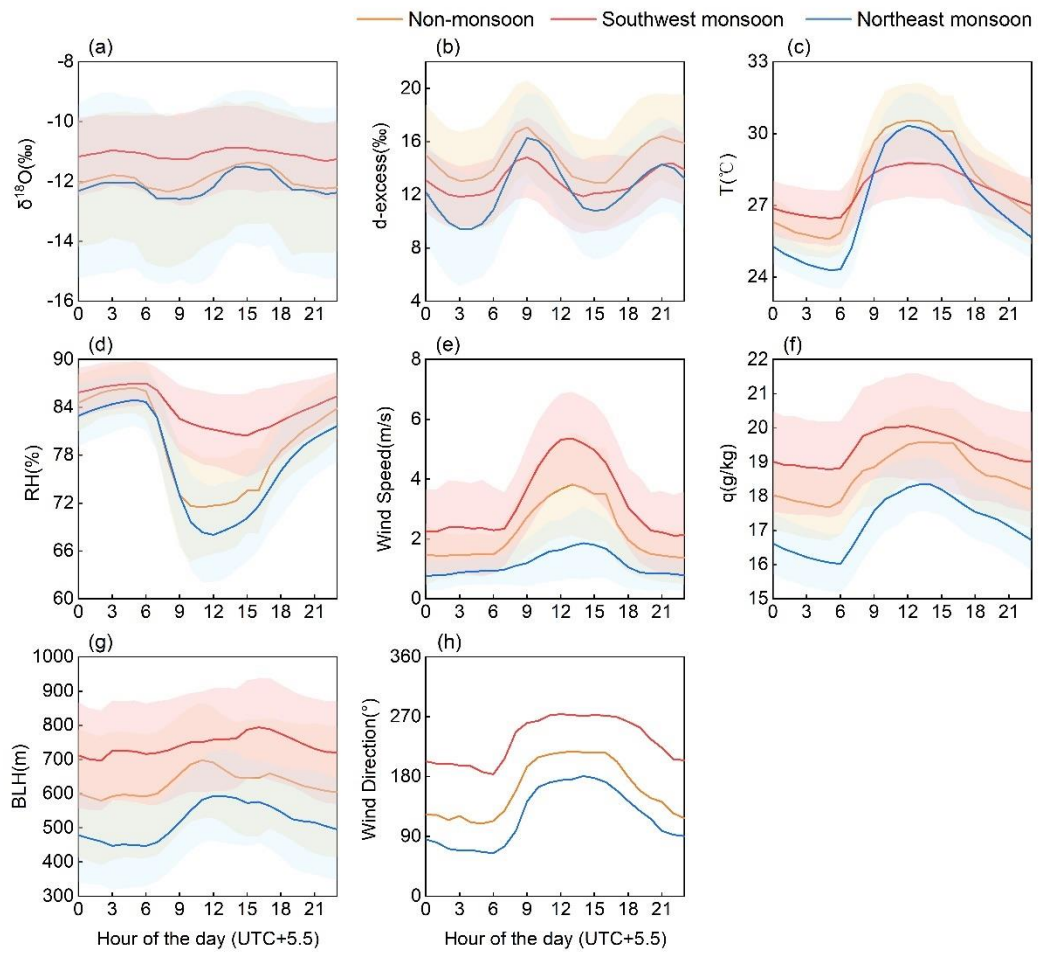
502 below the Rayleigh line. During the northeast monsoon, $\delta^{18}\text{O}$ spans from the upper to
503 the lower extreme of the mixing and Rayleigh distillation curves. The measurements
504 substantially deviate from the Rayleigh curve and show a higher depletion than
505 predicted by the Rayleigh model, likely due to the influence of convective processes.

506 **3.2 The Variation Characteristics of Diurnal Cycles**

507 To look for diurnal cycles in isotopic composition and meteorological parameters,
508 we analyzed hourly averages (Fig. 4c-e).

509 All isotopic ($\delta^{18}\text{O}$, δD , and d-excess) and meteorological parameters exhibit strong
510 diurnal variations during both monsoon and non-monsoon periods (Fig. 4). Overall, the
511 diurnal variations in local meteorological parameters of solar radiation during the day
512 and the resulting development of a boundary layer led to the increasing of temperature
513 and wind speed between the noon and afternoon, accompanied by a decrease in relative
514 humidity due to significant evapotranspiration. At night, surface radiative cooling
515 causes temperatures to drop, resulting in calmer conditions near the surface and gradual
516 air saturation, indicating a relatively stable atmospheric boundary layer. During the
517 southwest monsoon, $\delta^{18}\text{O}$, δD , relative humidity, wind speed, specific humidity, and
518 BLH are generally higher than during the northeast and non-monsoon periods, while d-
519 excess is lower. In the early morning, $\delta^{18}\text{O}$ steadily decreases, reaching a minimum (-
520 11.26‰) around sunrise (~09:00 local time (LT)). Subsequently, it increases throughout
521 the day, peaking (-10.87‰) in the afternoon (~15:00 LT), yielding a diurnal fluctuation
522 of merely 0.45‰. Increased specific humidity between 10:00 LT and 14:00 LT
523 coincides with increasing air temperatures and wind speeds and decreasing relative
524 humidity (Fig. 4c-f). BLH peaks between 14:00 LT and 16:00 LT, slightly later than
525 other meteorological parameters. The same diurnal variations for each parameter were
526 observed during the northeast monsoon, with maximum changes in $\delta^{18}\text{O}$ and d-excess
527 of 1.1‰ and 6.8‰, respectively. Specific humidity peaks between 10:00 LT and 16:00
528 LT, accompanied by increases in air temperature, wind speed, and BLH. After 16:00 LT,
529 specific humidity decreases alongside isotopic δ values and other meteorological
530 parameters. d-excess peaks (14.81‰) at 09:00 LT and fluctuates until 23:00 LT,

531 contrasting with the period from 04:00 LT to 09:00 LT (Fig. 4b). d-excess exhibits a W-
 532 shaped variability, reaching similar highs at 09:00 LT and 21:00 LT. Specific humidity
 533 exhibits a diurnal variation that aligns closely with the $\delta^{18}\text{O}$ pattern, reaching its
 534 minimum before sunrise and peaking around midday (10:00-15:00 LT). Between
 535 afternoon and evening, specific humidity remains relatively high and stable. The diurnal
 536 variation during the southwest and northeast monsoon periods are 1.28 g/kg and 2.32
 537 g/kg, respectively. Similarities with patterns observed at Lena River station in the
 538 eastern Siberia (Bonne et al. 2020) suggest potential influences from moisture exchange
 539 between the atmosphere and ocean surface, particularly during the northeast monsoon.



540

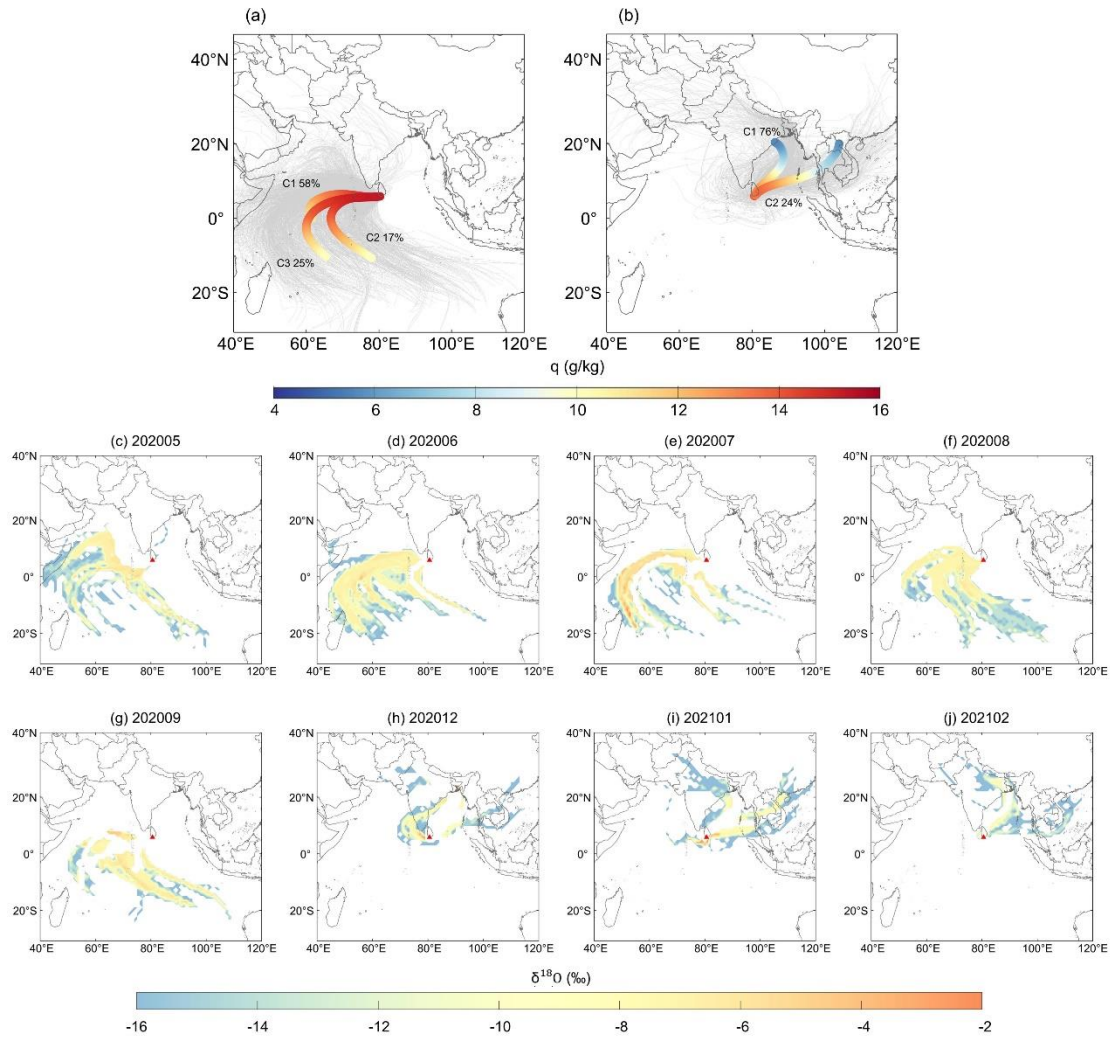
541 **Figure 4: Average diurnal cycles of (a) $\delta^{18}\text{O}$, (b) d-excess, (c) temperature (T), (d) relative**
 542 **humidity (RH), (e) wind speed, (f) specific humidity (q), (g) atmospheric boundary layer**
 543 **height (BLH), and (h) wind direction during the non-monsoon, southwest monsoon, and**
 544 **northeast monsoon periods. Shaded areas correspond to ± 1 standard deviation.**

545 **3.3 Sea Surface Evaporation Conditions in the Moisture Source**
546 **Region**

547 To be able to explore water vapor isotopic variations in the sea surface boundary
548 layer, we must first understand the processes and factors that affect isotope variations
549 during ocean surface water evaporation. The primary determinant governing water
550 vapor stable isotope shifts across different regions is the regional moisture transport
551 process, characterized by differences in isotopic variations in the moisture source
552 region, variations in meteorological conditions during the evaporation processes, and
553 divergences of the moisture transport pathways (Bonne et al., 2020). Thus, this section
554 aims to identify factors that drive the seasonal variations of near-surface atmospheric
555 water vapor stable isotopes at Matara, including water vapor origin, transmission routes,
556 and sea surface evaporation conditions in the source regions.

557 To further understand the different seasonal relationships between $\delta^{18}\text{O}$, d-excess,
558 and meteorological parameters, we analyzed potential seasonal differences between the
559 main moisture sources using HYSPLIT. Backward trajectories from the southwest and
560 northeast monsoons were spatially clustered and analyzed for changes in air mass
561 heights and specific humidity (Fig. S6), facilitating the identification of air mass origins.
562 The specific humidity along the path have been gridded, and we define the end points
563 of trajectories as the indicative of the moisture sources. Trajectories that reach Matara
564 during the southwest and northeast monsoons have different origins. During the
565 southwest monsoon, wind directions span from 60° to 360° and the main origin regions
566 are therefore the Arabian Sea (AS) and Indian Ocean (Fig. 5a). Due to the northward
567 movement of the warm South Equatorial Current, these winds gather significant
568 amounts of moisture along the way, bringing heavy rainfall to Matara (Fig. 5a and 5b).
569 Conversely, during the northeast monsoon, the main wind direction shifts to 0°-225°
570 and 330°-360°, such that most trajectories originate in northeast India, where specific
571 humidity is lower (overland), and only a short portion of the trajectory passes over the
572 BoB. The long transport distance results in a greater depletion in water vapor isotopes
573 once the air mass arrives at Matara station.

574 Moisture from all sources shows seasonal variations, with $\delta^{18}\text{O}$ values higher
 575 during the southwest monsoon than during the northeast monsoon. The shift in water
 576 vapor source from the AS in May to the southern Indian Ocean in September leads to
 577 $\delta^{18}\text{O}$ enriched water vapor from August to September. Enhanced convective activity
 578 and rainfall during the southwest monsoon result in $\delta^{18}\text{O}$ depletion, while tropical
 579 storms and hurricanes also contribute to $\delta^{18}\text{O}$ depletion.

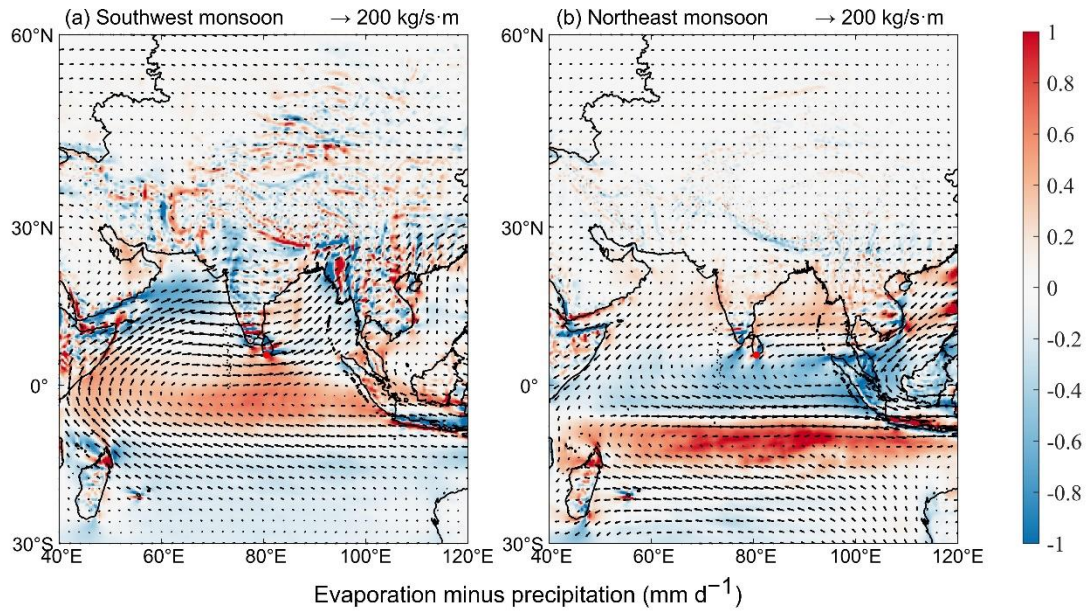


580 **Figure 5: Backward trajectories of water vapor tracks reaching Matara station and its four**
 581 **surrounding sites (heights: 50m, 500m, 1200m, and 2000m) during the (a) southwest monsoon**
 582 **and (b) northeast monsoon. The changes in specific humidity (q) along each clustered**
 583 **trajectory are shown in color. Numbers indicate the proportion (%) of trajectories represented**
 584 **by each clustered trajectory. Monthly concentration fields of water vapor isotopic $\delta^{18}\text{O}$ from**
 585 **a 168h HYSPLIT simulation of back trajectories during the two monsoon seasons (c-j). Red**

587 triangle marks the study site.

588 To assess how seasonal shifts in moisture sources impact the isotopic composition
589 of water vapor, we analyzed the relationship between specific humidity, isotope
590 variations, and wind direction at Matara station (Fig. S7). During the southwest
591 monsoon, wind directions were predominantly WNW, correlating with peak specific
592 humidity and highest $\delta^{18}\text{O}$ values and lowest d-excess, suggesting a westerly moisture
593 source. Conversely, air masses from the east exhibited $\delta^{18}\text{O}$ depletion and higher d-
594 excess. The northeast monsoon brought drier air from the BoB, leading to specific
595 humidity between 14 and 17 g/kg and significantly depleted $\delta^{18}\text{O}$ values. These air
596 masses likely experienced substantial isotopic fractionation during their overland
597 passage.

598 We also investigated the influence of water vapor flux, evaporation, and
599 precipitation on isotopic variations. The southwest monsoon saw lower evaporation
600 rates compared to precipitation at Matara station, contrasting with the northern Indian
601 Ocean and western BoB where evaporation surpassed precipitation. The northeast
602 monsoon, influenced by moisture from the BoB and South Asia, showed higher
603 evaporation rates, increasing water vapor flux. Overall, the water vapor flux and budget
604 varied markedly between monsoons, with the upstream vapor budget significantly
605 affecting stable isotope changes, particularly $\delta^{18}\text{O}$. The southwest monsoon's increased
606 precipitation and moisture transport from the northeast led to enriched $\delta^{18}\text{O}$ at Matara.
607 In contrast, the northeast monsoon's moisture transport resulted in a "washing effect",
608 causing a gradual $\delta^{18}\text{O}$ depletion due to continuous condensation and fractionation
609 along the transport pathway (Fig. 6 and S8).



610

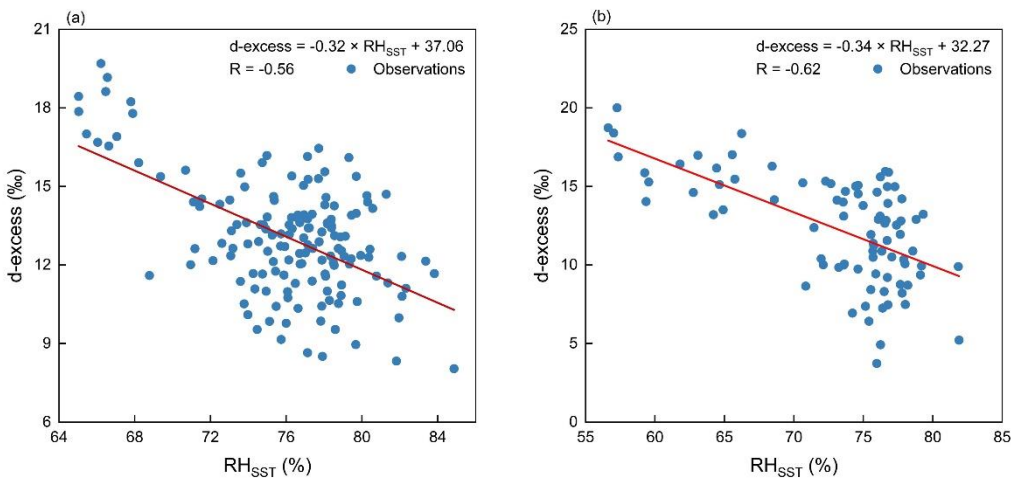
611 **Figure 6: Average water vapor flux and budget during the (a) southwest monsoon and (b)**
 612 **northeast monsoon, with the red dot marking Matara station.**

613 d-excess exhibits similar seasonal variations at Matara station, with lower values
 614 during the two monsoon seasons and higher values during the non-monsoon periods
 615 (Table 2, Fig. 4). This seasonal variation may stem from changes in relative humidity
 616 in the moisture source areas and further modifications during transport.

617 Ocean evaporation represents the starting point of the phase transformations that
 618 occur within the global water cycle. Identifying the isotopic variations and controlling
 619 factors of oceanic evaporation is essential for understanding isotopic shifts in the
 620 marine boundary layer. Previous coastal observational studies focusing on the marine
 621 boundary layer have confirmed a significant association between d-excess and RH_{SST}
 622 (Pfahl and Wernli, 2009; Steen-Larsen et al., 2015). In cases where kinetic fractionation
 623 during air mass transport is either absent or minimal, d-excess can serve as an indicator
 624 of the moisture source region (Bonne et al., 2014).

625 The map of the moisture sources (Fig. 5) identified the Indian Ocean and BoB as
 626 the main source areas for moisture arriving at Matara station. To gauge the impact of
 627 more local influences, we investigated how changes in sea surface meteorological
 628 conditions in the sea around Matara station affects near surface water vapor isotope
 629 concentrations (Fig. S9). During the southwest monsoon, RH_{SST} in "Region a" (located

630 to the south of Matara between 3-7°N and 56-65°E) ranged from 64% to 86%, with
 631 SST fluctuating between 27.9°C and 31.5°C. During the northeast monsoon, RH_{SST} in
 632 "Region b" (located to the east of Matara between 6-8°N and 82-85°E) ranged from 54%
 633 to 84%, with SST fluctuating between 28.1°C and 29.1°C. In comparison with the
 634 southwest monsoon, RH_{SST} is slightly lower, accompanied by less pronounced
 635 variability in SST. The rate of change in d-excess under the influence of RH_{SST} in the
 636 BoB (during the northeast monsoon) is -0.34 ‰/%. In comparison, the rate of change
 637 in d-excess with the RH_{SST} of the northern Indian Ocean (during the southwest monsoon)
 638 is -0.32 ‰/%, suggesting that evaporation over the northern Indian Ocean significantly
 639 impacts local d-excess. Studies focused on the BoB's sea surface revealed that RH_{SST}
 640 explains only 25% of the d-excess variation ($d\text{-excess} = (-0.55 \pm 0.14) \times RH_{SST} + (56 \pm 12)$;
 641 $r = -0.5$). The limited variation in relative humidity during the monsoon period
 642 led to a low correlation, indicating that monsoon moisture plays a crucial role in the
 643 isotopic composition of water vapor in the BoB (Midhun et al., 2013). Conversely, the
 644 observed relationship between near-surface water vapor d-excess at Matara and relative
 645 humidity in the surrounding oceanic region during the observational period, with
 646 correlation coefficients of -0.56 and -0.62 ($p < 0.01$), respectively (Fig. 7), reveals a
 647 marked negative correlation between d-excess and relative humidity in the nearby
 648 Indian Ocean and BoB, indicating that water vapor at Matara is predominantly supplied
 649 by nearby oceans. Notably, SST amplitude near the Matara station is smaller than the
 650 variations in near-surface air temperature (Fig. 2).



651

652 **Figure 7: Relationship between d-excess and RH_{SST} during the (a) southwest monsoon and (b)**
653 **northeast monsoon. Specific sea regions (Fig. S10) to the south (Region a: 3-7°N and 56-65°E)**
654 **and east (Region b: 6-8°N and 82-85°E) of the observation station were selected to investigate**
655 **the impact of sea surface meteorological conditions on near-surface water vapor isotopes**
656 **during the two monsoon periods.**

657 **3.4 The Influence of Regional Convective Activity**

658 In the equatorial tropics, OLR mainly results from convective activity and cloud
659 cover, which can impact the stable isotope composition of precipitation (Ohring et al.,
660 1984; Gao et al., 2013; Guo et al., 2017). Generally, higher OLR values are associated
661 with weaker convective activity. Examining the correlation between stable isotopes of
662 water vapor and OLR helps to understand the impact of convective activities along
663 near-surface trajectories of water vapor stable isotopes at Matara station.

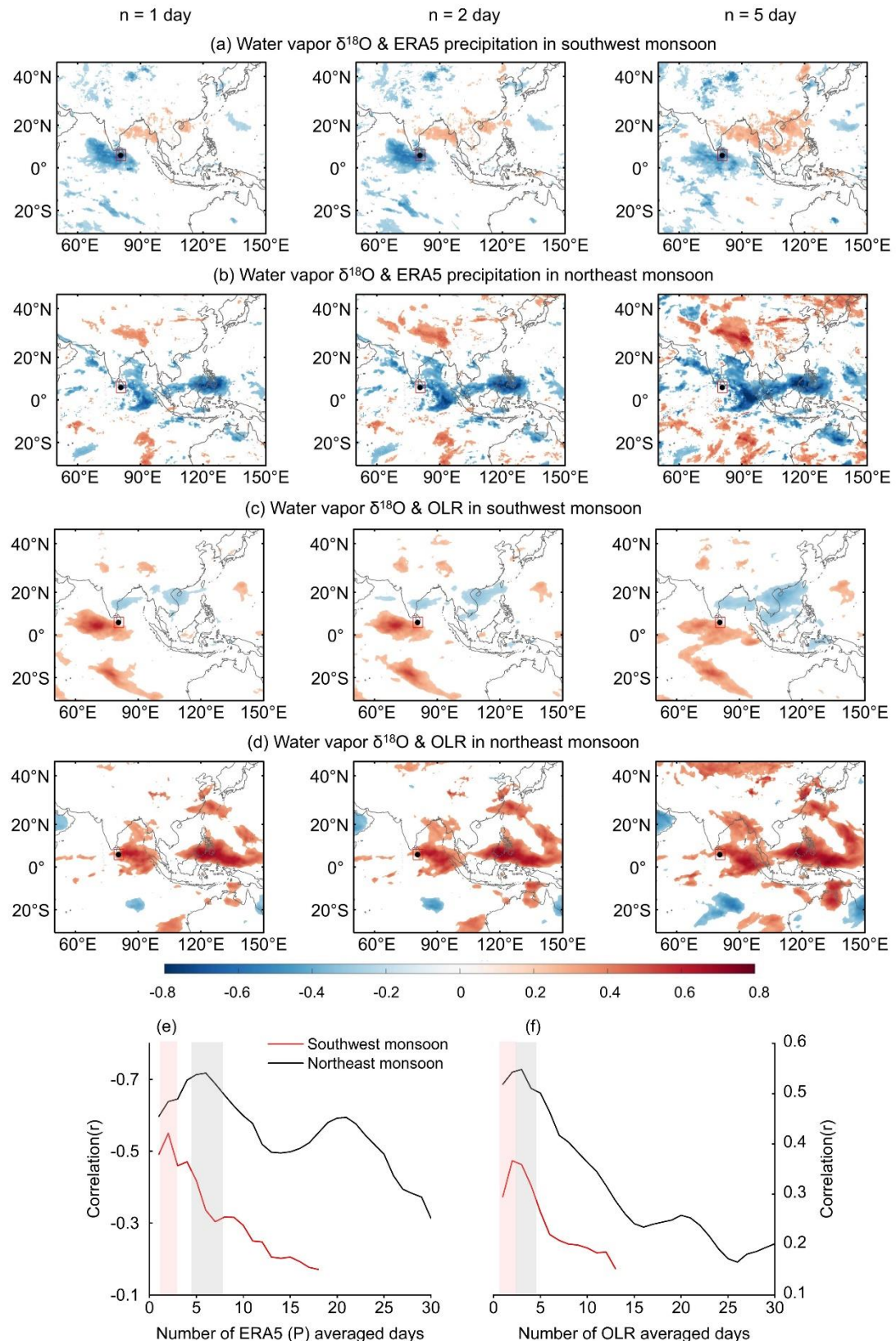
664 We calculated the spatiotemporal correlation between OLR and precipitation
665 amount using the measured water vapor isotopic compositions at Matara station.
666 Specifically, we calculated the average precipitation amount and average OLR for each
667 grid point by averaging over different numbers of days ($n = 1, 2$, up to 30) preceding
668 each day. Lower OLR values indicate the presence of deep convective clouds in this
669 region and higher precipitation associated with lower δ values.

670 Fig. 8a shows the strong positive correlation (red regions) between rainfall and
671 $\delta^{18}\text{O}$ during the southwest monsoon, mainly in the northern BoB and over India. This
672 correlation strengthens and extends over wider areas as n increases from 1 to 5.
673 Additionally, a strong negative correlation is evident in the northern Indian Ocean and
674 southern Arabian Sea, reaching a maximum for $n = 2$ d. During the northeast monsoon,
675 the spatial correlation distribution differs, with a negative correlation observed over the
676 southern Indian Ocean and BoB (Fig. 8b), reaching a maximum for $n = 5$ d. Lower OLR
677 values in the Arabian Sea and the northern part of the India Ocean correspond to a
678 decrease in water vapor isotopic $\delta^{18}\text{O}$ at Matara station (Fig. 8c, d). This pattern
679 indicates that water vapor $\delta^{18}\text{O}$ during the northeast monsoon period is influenced by
680 convective activities over the South BoB, and Southeast Asian regions. The stronger

681 this convective activity, the more depleted is the air reaching Matara in water vapor
682 isotopic $\delta^{18}\text{O}$.

683 To examine the correlation between water vapor isotopic $\delta^{18}\text{O}$ and local
684 precipitation (Fig. 8e) and OLR (Fig. 8f), we selected a small region of $5^\circ \times 5^\circ$ around
685 Matara and calculated the temporal correlation for all grid points as described above.
686 The results show that the correlation with precipitation is negative during both monsoon
687 seasons as expected. The depletion of low-level water vapor $\delta^{18}\text{O}$ is related to the
688 transport and deposition of water vapor into the lower atmosphere through convective
689 activity (Kurita, 2013; Midhun et al., 2013; Lekshmy et al., 2014). The air masses are
690 re-supplied to the convective system through moisture recycling. This results in a strong
691 correlation between the isotopic composition of water vapor and the convective activity
692 during the previous day (Fig. 8f). Residual water vapor is more depleted in strong
693 convective systems. In our study, the correlation reaches a high value after about 5 days,
694 indicating that the convective activity is sufficiently established to affect the isotopic
695 composition of water vapor. In fact, the correlation (for $p < 0.05$ and in absolute terms)
696 is high for all n values, with maxima of about 0.37 for $n = 2$ d during the southwest
697 monsoon and 0.55 for $n = 2$ to 5 d during the northeast monsoon.

698 The OLR correlation peaks at smaller time scales (approximately $n = 2$ -5 d, Fig.
699 8f) than precipitation ($n = 3$ -7 d). We attribute this difference to the effect of cloud
700 distribution on precipitation and OLR. OLR has a stronger response to shallow clouds,
701 while precipitation is more responsive to both deep convective clouds and shallow
702 clouds (Masunaga and Kummerow, 2006; Schumacher, 2006). The OLR minimum
703 occurs when thunderstorm clouds result in more precipitation. Additionally, deep
704 thunderstorm clouds, with short lifetimes and consequently very low OLR
705 (corresponding to highly depleted water vapor isotopic δ), exhibit a short memory effect
706 on the correlation (peak occurs at smaller time scales) (Gambheer and Bhat, 2000).



707

708

709

710

Figure 8: Isotopic composition correlations with precipitation and OLR during monsoon periods. (a, b): Spatial correlations between water vapor $\delta^{18}\text{O}$ and ERA5-precipitation for the southwest (a) and northeast (b) monsoons. (c, d): Spatial correlations between water vapor

711 **$\delta^{18}\text{O}$ and average OLR for the southwest (c) and northeast (d) monsoons. (e): Correlation**
712 **between $\delta^{18}\text{O}$ and ERA5-precipitation (P) across different averaging periods (n = 1 to 30 days)**
713 **for southwest (red line) and northeast (black line) monsoons. (f): Correlation between $\delta^{18}\text{O}$**
714 **and OLR across southwest (red line) and northeast (black line) monsoons over varying**
715 **averaging periods. Red areas indicate significant negative correlations, grey areas indicate**
716 **significant positive correlations.**

717 **Note: Only correlations surpassing the 99% confidence threshold are displayed. The red box**
718 **denotes the Matara station's region of interest.**

719

720 **4. Discussion: Comparing Main Features and Identifying Influencing** 721 **Factors**

722 This study presented the results from a one-year (March 2020 to February 2021)
723 in-situ measurement campaign of near-surface atmospheric water vapor isotopes ($\delta^{18}\text{O}$,
724 δD) at Matara station, Sri Lanka. These high-temporal resolution water vapor isotopic
725 composition and meteorological observations provided a good opportunity to
726 investigate the water vapor isotopic dynamics from synoptic to seasonal scales. The
727 variability of water vapor isotopes at Matara station is influenced by local
728 meteorological factors, oceanic evaporation processes, and regional convective
729 activities, depending on the water sources and moisture transport. The measurements
730 provided insights into multi-time-scale variations in near-surface atmospheric water
731 vapor in an equatorial region and provided information about the interactions between
732 large-scale atmospheric moisture transport and oceanic evaporation.

733 During the both monsoon periods, specific humidity and stable water isotope
734 composition showed a clear diurnal cycle at Matara station, primarily due to the
735 significant contribution of local evapotranspiration to the overall moisture balance. In
736 equatorial regions, seasonal variations in stable water vapor isotopes are largely
737 governed by changes moisture sources and the transport processes. Ponmudi station,
738 located in southern India (Lekshmy et al., 2018), shares many characteristics with
739 Matara station, in that it is also a coastal city, influenced by both the southwest and

740 northeast monsoons. During the summer, moisture sources for air arriving at Ponmudi
741 are mostly located in the southern Arabian Sea and equatorial Indian Ocean, with
742 relative humidity levels exceeding 70%. This high relative humidity, combined with a
743 continuous supply of moisture from the Arabian Sea, results in significant rainfall in
744 the Ponmudi region, exceeding 2040 mm per year.

745 Fluctuations of water vapor stable isotopes at shorter (weather) time scales are
746 closely associated with regional convective activities. Research conducted on
747 precipitation and water vapor stable isotopes at Bangalore, another coastal city in
748 southern India, indicates that local meteorological parameters do not influence isotope
749 ratios (Rahul et al., 2016b). Rather, these ratios are affected by the integrated regional
750 convective activity, characterized by large-scale rainfall or outgoing longwave radiation
751 flux. Like Matara station, Bangalore is also affected by both the southwest and northeast
752 monsoons. The observed depletion in heavy isotopes may be due to the influx of
753 moisture from the Bay of Bengal, depleted due to the rainout effect, mixing with air
754 that has travelled overland crossing the Indian subcontinent.

755 Overall, the long-term monitoring of water vapor stable isotopes in South Asian
756 equatorial regions could highlight the importance of both seasonal and sub-seasonal
757 (weather-scale) variations, mostly due to changes in moisture sources and processes
758 that occur during the air mass transport at the circulation scale. Matara station served
759 as a good location to study the effects of moisture transport processes over the Indian
760 Ocean. We could also identify seasonal patterns that in general agree with previous
761 findings for tropical equatorial regions (Midhun et al., 2013; Rahul et al., 2016b;
762 Lekshmy et al., 2018).

763

764 **5. Summary and Conclusions**

765 One-year (March 2020 to February 2021) in situ meteorological observations and
766 measurements of water vapor isotopic composition were conducted at Matara station,
767 Sri Lanka. Meteorological parameters exhibited diurnal variations during both
768 monsoon and non-monsoon periods. The new dataset provides detailed information on

769 the isotopic composition of near-surface atmospheric water vapor, which complements
770 local precipitation isotopic dataset by including periods without rainfall. Additionally,
771 it enables a comparative analysis of water vapor isotopic variations across the two
772 monsoon periods. Research findings indicate that during the northeast monsoon, diurnal
773 fluctuations in $\delta^{18}\text{O}$, temperature, and specific humidity were observed, with maximum
774 values reaching 1.1‰, 6.0°C, and 2.3 g/kg, respectively. In contrast, during the
775 southwest monsoon these parameters exhibit only small magnitude fluctuations of
776 0.45‰, 2.3°C, and 1.3 g/kg. Atmospheric temperature affects isotopic composition
777 through its effect on isotope fractionation. Additionally, a weak seasonal variability in
778 near-surface water vapor isotopes was observed, with $\delta^{18}\text{O}$ typically showing high
779 values (-11.1‰) during the monsoon period and low values (-11.9‰) during the non-
780 monsoon period. d-excess exhibited lower value (12.7‰) during the monsoon period
781 than during the non-monsoon period (14.7‰).

782 An evaluation of water vapor sources using HYSPLIT indicates small but notable
783 seasonal variations in air mass origins. The source regions differ seasonally, with the
784 northern Indian Ocean serving as the primary source during the southwest monsoon,
785 and the Bay of Bengal dominating as the source during the northeast monsoon.
786 Significant variations in water vapor flux and budget occur during the monsoon periods,
787 with upstream water vapor budgets exerting a pronounced impact on isotopic signatures,
788 especially $\delta^{18}\text{O}$. Evaporation over the northern Indian Ocean significantly impacts local
789 d-excess at Matara. Contrary to previous research indicating a weak correlation ($r = -$
790 0.5) between d-excess in the Bay of Bengal and the sea surface relative humidity (RH_{SST})
791 (Midhun et al., 2013), we found a slightly stronger negative correlation with RH_{SST}
792 during the monsoon periods, with values of -0.61 and -0.62 ($p < 0.01$) for the northern
793 Indian Ocean and Bay of Bengal, respectively. This study underscores the capability of
794 near-surface d-excess to reflect the evaporation conditions over these oceanic source
795 regions. However, ~~existing trajectory-based methods for identifying water vapor~~
796 ~~sources lack integration with mass-based water vapor budget analyses, and~~ the impact
797 of raindrop evaporation is yet to be thoroughly explored.

798 Consistent with previous research (Rahul et al., 2016b), large-scale rainfall and
799 regional convective activity (OLR) significantly impact isotope ratios at Matara station.
800 Notably, significant changes in $\delta^{18}\text{O}$ were observed during a heavy rainfall event in July
801 2020, with a sharp decline in isotopic values from $-10.4\text{\textperthousand}$ to $-20.4\text{\textperthousand}$ within 20 hours.
802 During the southwest monsoon, strong cloud cover and high humidity over the ocean
803 may lead to $\delta^{18}\text{O}$ enrichment at Matara station. The water vapor isotope compositions
804 observed during the southwest monsoon are similar as those observed in the Bay of
805 Bengal (Midhun et al., 2013). The depleted of water vapor isotope values at Matara
806 station in autumn and winter is consistent with findings from other coastal stations, such
807 as Bangalore, Ponmudi, and Wayanad (Rahul et al., 2016b; Lekshmy et al., 2018).
808 Current investigations into convection activities and evaporation processes in tropical
809 and subtropical regions offer fresh perspectives on the stable isotopic composition of
810 water vapor in these regions (Landshuter et al., 2024; Galewsky et al., 2023; Baily et
811 al., 2015). The re-evaporation of raindrops in deep convection (Risi et al., 2019) and
812 the formation of ice clouds in tropical regions (de Vries et al., 2022), which influence
813 the tropopause, provide critical insights into the factors governing isotopic variability
814 during shallow and deep convection. Simulations that incorporate entrainment and
815 mixing processes highlight the importance of accurately quantifying the effects of
816 hydrometeor evaporation on water vapor stable isotopes (Risi et al., 2019; Benetti et al.,
817 2015). These findings form a basis for deeper exploration of the distinctive isotopic
818 characteristics of tropical water vapor during the different monsoon periods. Our study
819 is the first to point out that the correlation between OLR and $\delta^{18}\text{O}$ peaks around 2-5
820 days before the observation, which we attribute to the impacts of cloud distribution.

821 This study examines the origins of moisture arriving at Matara station and the
822 associated atmospheric transport, with a focus on the substantial impact of cloud
823 distribution on the stable isotopic composition of water vapor, driven by regional
824 convection. Therefore, these insights are crucial for refining our grasp of isotopic
825 dynamics, particularly in relation to cloud microphysics and atmospheric mixing
826 processes within the broader water cycle (de Vries et al., 2022). This comprehensive

827 dataset containing synchronous water vapor isotope and meteorological measurements
828 offer extensive opportunities for further analyses, e.g., of the typical weather events,
829 atmospheric patterns, and ocean-atmosphere interactions in the equatorial region.
830 Given that only one year of observations is currently available, there is a pressing need
831 for supplementary and sustained measurements of water vapor stable isotopes in this
832 region to support multi-year studies and interannual variabilities. Furthermore, given
833 the anticipated changes in numerous weather and hydrological processes in equatorial
834 regions, future research should explore the impacts of typical weather events, and
835 ocean-atmosphere interactions, to deepen our understanding of extreme events and
836 large-scale atmospheric modes (e.g., ENSO, MJO, and IOD). Considering the temporal
837 and spatial variability in the dynamics of tropical ocean-atmosphere systems, high-
838 resolution isotope models and satellite datasets should be combined for a more
839 comprehensive analysis in the future.

840 **Acknowledgements:**

841 This work was funded by The Second Tibetan Plateau Scientific Expedition and
842 Research (STEP) program (Grant No. 2019QZKK0208) and the National Natural
843 Science Foundation of China (Grants 41922002 and 41988101-03), as well as the
844 Innovation Program for Young Scholars of TPESER (QNCX2022ZD-01). We thank
845 staff in the China Sri Lanka Joint Center for Education and Research, Mr. Charith
846 Madusanka Widanage, and Dr. Di Dai for their invaluable support and assistance with
847 measurements.

848

849 **Author Contributions:**

850 **Yuqing Wu****WYQ**: Data curation, Formal analysis, Writing - Original draft
851 preparation. **Jing Gao****GJ**: Data curation, Conceptualization, Methodology,
852 Supervision, Writing - Review and Editing, Funding acquisition. **Aibin Zhao****ZAB**:
853 Writing - Review and Editing, Project administration. **Xiaowei Niu****NXW**: Data
854 curation. **Yigang Liu****LYG**: Data curation. **Disna Ratnasekera****RD**: Project
855 administration. **Tilak Priyadarshana Gamage****GTP**: Project administration.
856 **Amarasinghe Hewage Ruwan Samantha****SAHR**: Data curation.

857

858 **Data availability:**

859 The ERA5 dataset is the latest reanalysis dataset published by the European Centre
860 for Medium-Range Weather Forecasts (ECMWF) (Hersbach et al., 2020)
861 (<https://cds.climate.copernicus.eu/cdsapp#!/home>). The Global Data Assimilation
862 System (GDAS) has been published by the US National Oceanic and Atmospheric
863 Administration (NOAA) (<ftp://arlftp.arlhq.noaa.gov/archives/gdas1/>). The water vapor
864 isotopic compositions dataset will be available on the Zenodo research data repository
865 after manuscript publication.

866

867 **Competing interests:**

868 The contact author has declared that none of the authors has any competing interests.

869 **References**

870 [Aemisegger, F., and Sjolte, J.: A Climatology of Strong Large-Scale Ocean Evaporation](#)
871 [Events. Part II: Relevance for the Deuterium Excess Signature of the](#)
872 [Evaporation Flux, J. Climate, 31, 7313-7336, https://doi.org/10.1175/JCLI-D-](#)
873 [17-0592.1, 2018.](#)

874 Aemisegger, F., Sturm, P., Graf, P., Sodemann, H., Pfahl, S., Knohl, A., and Wernli, H.:
875 Measuring variations of $\delta^{18}\text{O}$ and $\delta^2\text{H}$ in atmospheric water vapour using two
876 commercial laser-based spectrometers: an instrument characterisation study,
877 Atmos. Meas. Tech., 5, 1491-1511, <https://doi.org/10.5194/amt-5-1491-2012>,
878 2012.

879 Angert, A., Lee, J.E., and Yakir, D.: Seasonal variations in the isotopic composition of
880 near-surface water vapour in the eastern Mediterranean, Tellus B, 60, 674-684,
881 <https://doi.org/10.1111/j.1600-0889.2008.00357.x>, 2008.

882 Bailey, A., Aemisegger, F., Villiger, L., Los, S.A., Reverdin, G., Quiñones Meléndez,
883 E., Acquistapace, C., Baranowski, D.B., Böck, T., Bony, S., Bordsdorff, T.,
884 Coffman, D., de Szoke, S.P., Diekmann, C.J., Dütsch, M., Ertl, B., Galewsky,
885 J., Henze, D., Makuch, P., Noone, D., Quinn, P.K., Rösch, M., Schneider, A.,
886 Schneider, M., Speich, S., Stevens, B., and Thompson, E.J.: Isotopic
887 measurements in water vapor, precipitation, and seawater during EUREC4A,
888 Earth Syst. Sci. Data, 15, 465-495, <https://doi.org/10.5194/essd-15-465-2023>,
889 2023.

890 Bailey, H.L., Kaufman, D.S., Henderson, A.C.G., Leng, M.J.: Synoptic scale controls
891 on the $\delta^{18}\text{O}$ in precipitation across Beringia, Geophys. Res. Lett., 42, 4608-
892 4616, <https://doi.org/10.1002/2015GL063983>, 2015.

893 Bandara, U., Agarwal, A., Srinivasan, G., Shanmugasundaram, J., and Jayawardena,
894 I.M.S.: Intercomparison of gridded precipitation datasets for prospective
895 hydrological applications in Sri Lanka, Int. J. Climatol., 42, 3378-3396,

896 <https://doi.org/10.1002/joc.7421>, 2022.

897 Bavadekar, S.N., and Mooley, D.A.: Use of the equation of continuity of water vapour
898 for computation of average precipitation over peninsular India during the
899 summer monsoon, In: Lighthill, J., Pearce, P.R. (Eds.), Monsoon Dynamics,
900 Cambridge University Press, Cambridge, pp., 261-268, 1981.

901 Bedaso, Z., and Wu, S-Y.: Daily precipitation isotope variation in Midwestern United
902 States: Implication for hydroclimate and moisture source, *Sci. Total Environ.*,
903 713, 136631, <https://doi.org/10.1016/j.scitotenv.2020.136631>, 2020.

904 Benetti, M., Aloisi, G., Reverdin, G., Risi, C., and Sèze, G.: Importance of boundary
905 layer mixing for the isotopic composition of surface vapor over the subtropical
906 North Atlantic Ocean, *J. Geophys. Res. Atmos.*, 120, 2190-2209,
907 <https://doi.org/10.1002/2014JD021947>, 2015.

908 Benetti, M., Lacour, J-L., Sveinbjörnsdóttir, A.E., Aloisi, G., Reverdin, G., Risi, C.,
909 Peters, A.J., and Steen-Larsen, H.C.: A Framework to Study Mixing Processes
910 in the Marine Boundary Layer Using Water Vapor Isotope Measurements,
911 *Geophys. Res. Lett.*, 45(5), 2524-2532, <https://doi.org/10.1002/2018GL077167>,
912 2018.

913 Benetti, M., Reverdin, G., Pierre, C., Merlivat, L., Risi, C., Steen-Larsen, H.C., and
914 Vimeux, F.: Deuterium excess in marine water vapor: Dependency on relative
915 humidity and surface wind speed during evaporation, *J. Geophys. Res. Atmos.*,
916 119, 584-593, <https://doi.org/10.1002/2013JD020535>, 2014.

917 Bhattacharya, S., Pal, M., Panda, B., and Pradhan, M.: Spectroscopic investigation of
918 hydrogen and triple-oxygen isotopes in atmospheric water vapor and
919 precipitation during Indian monsoon season, *Isot. Environ. Health. S.*, 57, 368-
920 385, <https://doi.org/10.1080/10256016.2021.1931169>, 2021.

921 Blossey, P.N., Kuang, Z., and Romps, D.M.: Isotopic composition of water in the
922 tropical tropopause layer in cloud-resolving simulations of an idealized tropical
923 circulation, J. Geophys. Res. Atmos., 115, D24309, doi:
924 <https://doi.org/10.1029/2010JD014554>, 2010.

925 Bonne, J-L., Behrens, M., Meyer, H., Kipfstuhl, S., Rabe, B., Schönicke, L., Steen-
926 Larsen, H.C., and Werner, M.: Resolving the controls of water vapour isotopes
927 in the Atlantic sector, *Nat. Commun.*, 10, 1632, <https://doi.org/10.1038/s41467-019-09242-6>, 2019.

928

929 Bonne, J-L., Masson-Delmotte, V., Cattani, O., Delmotte, M., Risi, C., Sodemann, H.,
930 and Steen-Larsen, H.C.: The isotopic composition of water vapour and
931 precipitation in Ivittuut, Southern Greenland, *Atmos. Chem. Phys.*, 14, 4419-
932 2014, <https://doi.org/10.5194/acp-14-4419-2014>, 2014.

933 Bonne, J-L., Meyer, H., Behrens, M., Boike, J., Kipfstuhl, S., Rabe, B., Schmidt, T.,
934 Schönicke, L., Steen-Larsen, H.C., and Werner, M.: Moisture origin as a driver
935 of temporal variabilities of the water vapour isotopic composition in the Lena
936 River Delta, Siberia, *Atmos. Chem. Phys.*, 20, 10493-10511,
937 <https://doi.org/10.5194/acp-20-10493-2020>, 2020.

938 Bookhagen, B., and Burbank, D.W.: Toward a complete Himalayan hydrological
939 budget: Spatiotemporal distribution of snowmelt and rainfall and their impact
940 on river discharge, *J. Geophys. Res.*, 115, F03019,
941 <https://doi.org/10.1029/2009JF001426>, 2010.

942 Cai, Z., Tian, L., and Bowen, G.J.: ENSO variability reflected in precipitation oxygen
943 isotopes across the Asian Summer Monsoon region, *Earth Planet. Sci. Lett.*, 475,
944 25-33, <https://doi.org/10.1016/j.epsl.2017.06.035>, 2017.

945 Cai, Z., and Tian, L.: Atmospheric Controls on Seasonal and Interannual Variations in
946 the Precipitation Isotope in the East Asian Monsoon Region, *J. Climate*, 29,
947 1339-1352, <https://doi.org/10.1175/JCLI-D-15-0363.1>, 2016.

948 Chakraborty, S., Sinha, N., Chattopadhyay, R., Sengupta, S., Mohan, P.M., and Datye,
949 A.: Atmospheric controls on the precipitation isotopes over the Andaman
950 Islands, Bay of Bengal, *Sci. Rep.*, 6, 19555, <https://doi.org/10.1038/srep19555>,
951 2016.

952 Craig, H.: Isotopic Variation in Meteoric Waters. *Science*, 133, 1702-1703,
953 <https://doi.org/10.1126/science.133.3465.1702>, 1961.

954 Craig, H., and Gordon, L.I.: Deuterium and oxygen 18 variation in the ocean and the
955 marine atmosphere, In: Tongiorgi, E. (Eds.), Stable Isotopes in Oceanographic
956 Studies and Paleotemperatures, pp., 9-130, 1965.

957 Curry, J.A., and Webster, P.J.: Thermodynamics of Atmospheres and Oceans, Academic
958 Press, London, 31705, 1999.

959 Dai, D., Gao, J., Steen-Larsen, H.C., Yao, T., Ma, Y., Zhu, M., and Li, S.: Continuous
960 monitoring of the isotopic composition of surface water vapor at Lhasa,
961 southern Tibetan Plateau, Atmos. Res., 264, 105827,
962 <https://doi.org/10.1016/j.atmosres.2021.105827>, 2021.

963 Dansgaard, W.F.: Stable Isotopes in Precipitation, Tellus B, 16, 436-468,
964 <https://doi.org/10.1111/j.2153-3490.1964.tb00181.x>, 1964.

965 Delattre, H., Vallet-Couïn, C., and Sonzogni, C.: Deuterium excess in the
966 atmospheric water vapour of a Mediterranean coastal wetland: regional vs. local
967 signatures, Atmos. Chem. Phys., 15, 10167-10181, <https://doi.org/10.5194/acp-15-10167-2015>, 2015.

968 de Vries, A.J., Aemisegger, F., Pfahl, S., and Wernli, H.: Stable water isotope signals in
969 tropical ice clouds in the West African monsoon simulated with a regional
970 convection-permitting model, Atmos. Chem. Phys., 22, 8863-8895,
971 <https://doi.org/10.5194/acp-22-8863-2022>, 2022.

972 Dhar, O., and Rakhecha, P.: Foreshadowing Northeast Monsoon Rainfall Over Tamil
973 Nadu, India, Mon. Weather Rev., 111, 109, [https://doi.org/10.1175/1520-0493\(1983\)111<0109:FNMROT>2.0.CO;2](https://doi.org/10.1175/1520-0493(1983)111<0109:FNMROT>2.0.CO;2), 1983.

974 Diekmann, C.J., Schneider, M., Knippertz, P., de Vries, A.J., Pfahl, S., Aemisegger, F.,
975 Dahinden, F., Ertl, B., Khosrawi, F., Wernli, H., and Braesicke, P.: A Lagrangian
976 Perspective on Stable Water Isotopes During the West African Monsoon, J.
977 Geophys. Res. Atmos., 126, e2021JD034895,
978 <https://doi.org/10.1029/2021JD034895>, 2021.

979 Düttsch, M., Pfahl, S., Meyer, M., and Wernli, H.: Lagrangian process attribution of
980 isotopic variations in near-surface water vapour in a 30-year regional climate

983 simulation over Europe, *Atmos. Chem. Phys.*, 18, 1653-1669,
984 <https://doi.org/10.5194/acp-18-1653-2018>, 2018.

985 Gadgil, S.: The Indian Monsoon and Its Variability, *Rev. Earth Pl. Sci.*, 31, 429-467,
986 <https://doi.org/10.1146/annurev.earth.31.100901.141251>, 2003.

987 Galewsky, J., and Hurley, J.V.: An advection-condensation model for subtropical water
988 vapor isotopic ratios, *J. Geophys. Res. Atmos.*, 115, 116,
989 <https://doi.org/10.1029/2009JD013651>, 2010.

990 Galewsky, J., Schneider, M., Diekmann, C., Semie, A., Bony, S., Risi, C., Emanuel, K.,
991 Brogniez, H.: The Influence of Convective Aggregation on the Stable Isotopic
992 Composition of Water Vapor, *AGU Advances*, 4, e2023AV000877,
993 <https://doi.org/10.1029/2023AV000877>, 2023.

994 Galewsky, J., Steen-Larsen, H.C., Field, R.D., Worden, J., Risi, C., and Schneider, M.:
995 Stable isotopes in atmospheric water vapor and applications to the hydrologic
996 cycle, *Rev. Geophy.*, 54, 809-865, <https://doi.org/10.1002/2015RG000512>,
997 2016.

998 Gambheer, A.V., and Bhat, G.S.: Life Cycle Characteristics of Deep Cloud Systems
999 over the Indian Region Using INSAT-1B Pixel Data, *Mon. Weather Rev.*, 128,
1000 4071-4083, [https://doi.org/10.1175/1520-0493\(2000\)129<4071:LCCODC>2.0.CO;2](https://doi.org/10.1175/1520-0493(2000)129<4071:LCCODC>2.0.CO;2), 2000.

1002 Gao, J., Masson-Delmotte, V., Risi, C., He, Y., and Yao, T.: What controls precipitation
1003 $\delta^{18}\text{O}$ in the southern Tibetan Plateau at seasonal and intra-seasonal scales? A
1004 case study at Lhasa and Nyalam, *Tellus B*, 65, 21043,
1005 <https://doi.org/10.3402/tellusb.v65i0.21043>, 2013.

1006 Gao, Y., Li, X., Leung, L. R., Chen, D., and Xu, J.: Aridity changes in the Tibetan
1007 Plateau in a warming climate, *Environ. Res. Lett.*, 9, 104013,
1008 <https://doi.org/10.1088/1748-9326/10/3/034013>, 2014.

1009 Gat, J.: Oxygen and hydrogen isotopes in the hydrologic cycle, *Annu. Rev. Earth Pl.
1010 Sci.*, 24, 225-262, <https://doi.org/10.1146/ANNUREV.EARTH.24.1.225>, 1996.

1011 Gedzelman, S., Lawrence, J., Gamache, J., Black, M., Hindman, E., Black, R., Dunion,

1012 J., Willoughby, H., and Zhang, X.: Probing hurricanes with stable isotopes of
1013 rain and water vapor, *Mon. Weather Rev.*, 131, 1112-1127,
1014 [https://doi.org/10.1175/1520-0493\(2003\)131<1112:Phwsio>2.0.Co;2](https://doi.org/10.1175/1520-0493(2003)131<1112:Phwsio>2.0.Co;2), 2003.

1015 Goff, J.A., and Gratch, S.: Low-pressure properties of water from -160°F to 212 °F.
1016 *Transactions of the American Society of Heating and Ventilating Engineers*, 52,
1017 95-122, 1946.

1018 Goswami, B.N., Venugopal, V., Sengupta, D., Madhusoodanan, M.S., and Xavier, P.K.:
1019 Increasing Trend of Extreme Rain Events Over India in a Warming Environment,
1020 *Science*, 314, 1442-1445, <https://doi.org/10.1126/science.1132027>, 2006.

1021 Graf, P., Wernli, H., Pfahl, S., and Sodemann, H.: A new interpretative framework for
1022 below-cloud effects on stable water isotopes in vapour and rain, *Atmos. Chem.*
1023 *Phys.*, 19, 747-765, <https://doi.org/10.5194/acp-19-747-2019>, 2019.

1024 Guo, X., Tian, L., Wen, R., Yu, W., and Qu, D.: Controls of precipitation $\delta^{18}\text{O}$ on the
1025 northwestern Tibetan Plateau: A case study at Ngari station, *Atmos. Res.*, 189,
1026 141-151, <https://doi.org/10.1016/j.atmosres.2017.02.004>, 2017.

1027 Hersbach, H., Bell, B., Berrisford, P., Hirahara, S., Horányi, A., Muñoz Sabater, J.,
1028 Nicolas, J., Peubey, C., Radu, R., Schepers, D., Simmons, A., Soci, C., Abdalla,
1029 S., Abellán, X., Balsamo, G., Bechtold, P., Biavati, G., Bidlot, J., Bonavita, M.,
1030 and Thépaut, J.N.: The ERA5 global reanalysis, *Q. J. Roy. Meteor. Soc.*,
1031 <https://doi.org/10.1002/qj.3803>, 2020.

1032 Hsu, Y-K., Holsen, T.M., and Hopke, P.K.: Comparison of hybrid receptor models to
1033 locate PCB sources in Chicago, *Atmos. Environ.*, 37, 545-562,
1034 [https://doi.org/10.1016/S1352-2310\(02\)00886-5](https://doi.org/10.1016/S1352-2310(02)00886-5), 2003.

1035 Jayasena, H.A.H., Chandrajith, R., and Dissanayake, C.B.: Spatial variation of isotope
1036 composition in precipitation in a tropical environment: a case study from the
1037 Deduru Oya river basin, Sri Lanka, *Hydrol. Process.*, 22, 4565-4570,
1038 <https://doi.org/10.1002/hyp.7060>, 2008.

1039 Kaushal, N., Breitenbach, S.F.M., Lechleitner, F.A., Sinha, A., Tewari, V.C., Ahmad,
1040 S.M., Berkelhammer, M., Band, S., Yadava, M., Ramesh, R., and Henderson,

1041 G.M.: The Indian Summer Monsoon from a Speleothem $\delta^{18}\text{O}$ Perspective-A
1042 Review, Quaternary, 1, 29, <https://doi.org/10.3390/quat1030029>, 2018.

1043 Kostrova, S.S., Meyer, H., Fernandoy, F., Werner, M., and Tarasov, P.E.: Moisture
1044 origin and stable isotope characteristics of precipitation in southeast Siberia,
1045 Hydrol. Process., 34, 51-67, <https://doi.org/10.1002/hyp.13571>, 2020.

1046 Kurita, N.: Origin of Arctic water vapor during the ice-growth season, Geophys. Res.
1047 Lett., 38, <https://doi.org/10.1029/2010GL046064>, 2011.

1048 Kurita, N.: Water isotopic variability in response to mesoscale convective system over
1049 the tropical ocean, J. Geophys. Res. Atmos., 118, 10,376-10,390,
1050 <https://doi.org/10.1002/jgrd.50754>, 2013.

1051 Landshuter, N., Aemisegger, F., Mölg, T.: Stable Water Isotope Signals and Their
1052 Relation to Stratiform and Convective Precipitation in the Tropical Andes, J.
1053 Geophys. Res. Atmos., 129, e2023JD040630,
1054 <https://doi.org/10.1029/2023JD040630>, 2024.

1055 Lekshmy, P.R., Midhun, M., and Ramesh, R.: Influence of stratiform clouds on δD and
1056 $\delta^{18}\text{O}$ of monsoon water vapour and rain at two tropical coastal stations, J.
1057 Hydrol, 563, 354-362, <https://doi.org/10.1016/j.jhydrol.2018.06.001>, 2018.

1058 Lekshmy, P.R., Midhun, M., and Ramesh, R.: Role of moisture transport from Western
1059 Pacific region on water vapor isotopes over the Bay of Bengal, Atmos. Res.,
1060 265, 105895, <https://doi.org/10.1016/j.atmosres.2021.105895>, 2022.

1061 Lekshmy, P.R., Midhun, M., Ramesh, R., and Jani, R.A.: ^{18}O depletion in monsoon rain
1062 relates to large scale organized convection rather than the amount of rainfall,
1063 Sci. Rep., 4, 5661, <https://doi.org/10.1038/srep05661>, 2014.

1064 Liu, J., Ding, M., and Xiao, C.: Review on atmospheric water vapor isotopic
1065 observation and research: theory, method and modeling, Prog. Geog., 34, 340-
1066 353, <https://doi.org/10.11820/dlkxjz.2015.03.009>, 2015.

1067 Liu, X., and Chen, B.: Climatic warming in the Tibetan Plateau during recent decades,
1068 Int. J. Climatol., 20, 1729-1742, [https://doi.org/10.1002/1097-0088\(20001130\)20:14<1729::AID-JOC556>3.0.CO;2-Y](https://doi.org/10.1002/1097-0088(20001130)20:14<1729::AID-JOC556>3.0.CO;2-Y), 2000.

1070 Majoube, M.: Fractionnement en oxygène 18 entre la glace et la vapeur d'eau, Journal
1071 De Chimie Physique, 68, 625-636, 1971a.

1072 Majoube, M.: Fractionnement en oxygène 18 et en deutérium entre l'eau et sa vapeur,
1073 Journal de Chimie Physique et de Physico Chimie Biologique, 68, 1423-1436,
1074 <https://doi.org/10.1051/jcp/1971681423>, 1971b.

1075 Malmgren, B.A., Hulugalla, R., Hayashi, Y., and Mikami, T.: Precipitation trends in Sri
1076 Lanka since the 1870s and relationships to El Niño-southern oscillation, Int. J.
1077 Climatol., 23, 1235-1252, <https://doi.org/10.1002/joc.921>, 2003.

1078 Masunaga, H., and Kummerow, C.: Observations of tropical precipitating clouds
1079 ranging from shallow to deep convective systems, Geophys. Res. Lett., 33, 805,
1080 <https://doi.org/10.1029/2006GL026547>, 2006.

1081 Merlivat, L., and Jouzel, J.: Global climatic interpretation of the deuterium-oxygen 18
1082 relationship for precipitation, J. Geophys. Res. Oceans., 84, 5029-5033.
1083 <https://doi.org/10.1029/JC084iC08p05029>, 1979.

1084 Midhun, M., Lekshmy, P.R., and Ramesh, R.: Hydrogen and oxygen isotopic
1085 compositions of water vapor over the Bay of Bengal during monsoon, Geophys.
1086 Res. Lett., 40, 6324-6328, <https://doi.org/10.1002/2013GL058181>, 2013.

1087 Ohring, G., Gruber, A., and Ellingson, R.: Satellite Determinations of the Relationship
1088 between Total Longwave Radiation Flux and Infrared Window Radiance, J.
1089 Appl. Meteorol. Clim., 23, 416-425, [https://doi.org/10.1175/1520-0450\(1984\)023<0416:SDOTRB>2.0.CO;2](https://doi.org/10.1175/1520-0450(1984)023<0416:SDOTRB>2.0.CO;2), 1984.

1091 Pang, Z., Kong, Y., Froehlich, K., Huang, T., Yuan, L., Li, Z., and Wang, F.: Processes
1092 affecting isotopes in precipitation of an arid region, Tellus B, 63, 352-359,
1093 <https://doi.org/10.1111/j.1600-0889.2011.00532.x>, 2011.

1094 Permana, D.S., Thompson, L.G., and Setyadi, G.: Tropical West Pacific moisture
1095 dynamics and climate controls on rainfall isotopic ratios in southern Papua,
1096 Indonesia, J. Geophys. Res. Atmos., 121, 2222-2245,
1097 <https://doi.org/10.1002/2015JD023893>, 2016.

1098 Pfahl, S., and Wernli, H.: Air parcel trajectory analysis of stable isotopes in water vapor

1099 in the eastern Mediterranean, *J. Geophys. Res.*, 113, D20104,
1100 <https://doi.org/10.1029/2008JD009839>, 2008.

1101 Pfahl, S., and Wernli, H.: Lagrangian simulations of stable isotopes in water vapor: An
1102 evaluation of nonequilibrium fractionation in the Craig-Gordon model, *J.*
1103 *Geophys. Res. Atmos.*, 114, 108, <https://doi.org/10.1029/2009JD012054>, 2009.

1104 Rahul, P., Ghosh, P., and Bhattacharya, S.K.: Rainouts over the Arabian Sea and
1105 Western Ghats during moisture advection and recycling explain the isotopic
1106 composition of Bangalore summer rains, *J. Geophys. Res. Atmos.*, 121, 6148-
1107 6163, <https://doi.org/10.1002/2015JD024579>, 2016a.

1108 Rahul, P., Ghosh, P., Bhattacharya, S.K., and Yoshimura, K.: Controlling factors of
1109 rainwater and water vapor isotopes at Bangalore, India: Constraints from
1110 observations in 2013 Indian monsoon, *J. Geophys. Res. Atmos.*, 121, 13,936-
1111 13,952, <https://doi.org/10.1002/2016JD025352>, 2016b.

1112 Ranjan, S., Al, R., Keesari, T., Singh, V., Kumar, P., and Manish Leuenberger, M.: Triple
1113 Water Vapour-Isotopologues Record from Chhota Shigri, Western Himalaya,
1114 India: A Unified Interpretation based on $\delta^{17}\text{O}$, $\delta^{18}\text{O}$, δD and Comparison to
1115 Meteorological Parameters, *Front. Earth Sci.*, 8, 599-632,
1116 <https://doi.org/10.3389/feart.2020.599632>, 2021.

1117 Ravisankar, L., Madhavan, M., and Ramesh, R.: Spatial variation of amount effect over
1118 peninsular India and Sri Lanka: Role of seasonality, *Geophys. Res. Lett.*, 42,
1119 5500-5507, <https://doi.org/10.1002/2015GL064517>, 2015.

1120 Risi, C., Bony, S., and Vimeux, F.: Influence of convective processes on the isotopic
1121 composition ($\delta^{18}\text{O}$ and δD) of precipitation and water vapor in the tropics: 2.
1122 Physical interpretation of the amount effect, *J. Geophys. Res. Atmos.*, 113, 306,
1123 <https://doi.org/10.1029/2008JD009943>, 2008.

1124 Risi, C., Galewsky, J., Reverdin, G., Brient, F.: Controls on the water vapor isotopic
1125 composition near the surface of tropical oceans and role of boundary layer
1126 mixing processes, *Atmos. Chem. Phys.*, 19, 19, <https://doi.org/10.5194/acp-19-12235-2019>, 2019.

1128 Risi, C., Muller, C., and Blossey, P.: What controls the water vapor isotopic composition
1129 near the surface of tropical oceans? Results from an analytical model
1130 constrained by large-eddy simulations. *J. Adv. Model. Earth Sy.*, 12,
1131 e2020MS002106, [https://doi.org/10.1029/2020MS002106, 2020.](https://doi.org/10.1029/2020MS002106)

1132 Salamalikis, V., Argiriou, A.A., and Dotsika, E.: Stable isotopic composition of
1133 atmospheric water vapor in Patras, Greece: A concentration weighted trajectory
1134 approach, *Atmos. Res.*, 152, 93-104,
1135 <https://doi.org/10.1016/j.atmosres.2014.02.021>, 2015.

1136 Saranya, P., Krishan, G., Rao, M.S., Kumar, S., and Kumar, B.: Controls on water vapor
1137 isotopes over Roorkee, India: Impact of convective activities and depression
1138 systems, *J. Hydrol.*, 557, 679-687,
1139 <https://doi.org/10.1016/j.jhydrol.2017.12.061>, 2018.

1140 Schumacher, C.: Shallow tropical convection: How often does it rain? *Bull. Am.*
1141 *Meteorol. Soc.*, 87, 23-25, 2006.

1142 Singh, P., and Bengtsson, L.: Hydrological sensitivity of a large Himalayan basin to
1143 climate change, *Hydrol. Process.*, 18, 2363-2385,
1144 <https://doi.org/10.1002/hyp.1468>, 2004.

1145 Srivastava, R., Ramesh, R., Gandhi, N., Jani, R.A., and Singh, A.K.: Monsoon onset
1146 signal in the stable oxygen and hydrogen isotope ratios of monsoon vapor,
1147 *Atmos. Environ.*, 108, 117-124,
1148 <https://doi.org/10.1016/j.atmosenv.2015.02.062>, 2015.

1149 Steen-Larsen, H.C., Masson-Delmotte, V., Hirabayashi, M., Winkler, R., Satow, K.,
1150 Prié, F., Bayou, N., Brun, E., Cuffey, K., Dahl-Jensen, D., Dumont, M.,
1151 Guillevic, M., Kipfstuhl, J., Landais, A., Popp, T., Risi, C., Steffen, K., Stenni,
1152 B., and Sveinbjörnsdóttir, A.: What controls the isotopic composition of
1153 Greenland surface snow? *Clim. Past.*, 10, 379-392, <https://doi.org/10.5194/cpd-9-6035-2013>, 2013a.

1155 Steen-Larsen, H.C., Johnsen, S.J., Masson-Delmotte, V., Stenni, B., Risi, C., Sodemann,
1156 H., Balslev-Clausen, D., Blunier, T., Dahl-Jensen, D., Ellehøj, M.D., Falourd,

1157 S., Grindsted, A., Gkinis, V., Jouzel, J., Popp, T., Sheldon, S., Simonsen, S.B.,
1158 Sjolte, J., Steffensen, J.P., Sperlich, P., Sveinbjörnsdóttir, A.E., Vinther, B.M.,
1159 and White, J.W.C.: Continuous monitoring of summer surface water vapor
1160 isotopic composition above the Greenland Ice Sheet, *Atmos. Chem. Phys.*, 13,
1161 4815-4828, <https://doi.org/10.5194/acp-13-4815-2013>, 2013b.

1162 [Steen-Larsen, H.C., Risi, C., Werner, M., Yoshimura, K., and Masson-Delmotte, V.:](#)
1163 [Evaluating the skills of isotope-enabled general circulation models against in](#)
1164 [situ atmospheric water vapor isotope observations, J. Geophys. Res. Atmos.,](#)
1165 [122, 246–263, https://doi.org/10.1002/2016JD025443, 2017.](#)

1166 Steen-Larsen, H.C., Sveinbjörnsdóttir, A.E., Jonsson, T., Ritter, F., Bonne, J-L.,
1167 Masson-Delmotte, V., Sodemann, H., Blunier, T., Dahl-Jensen, D., and Vinther,
1168 B.M.: Moisture sources and synoptic to seasonal variability of North Atlantic
1169 water vapor isotopic composition, *J. Geophys. Res. Atmos.*, 120, 5757-5774,
1170 <https://doi.org/10.1002/2015JD023234>, 2015.

1171 Stewart, M.K.: Stable isotope fractionation due to evaporation and isotopic exchange
1172 of falling waterdrops: Applications to atmospheric processes and evaporation of
1173 lakes, *J. Geophys. Res.*, 80, 1133-1146,
1174 <https://doi.org/10.1029/JC080i009p01133>, 1975.

1175 Sturm, P., and Knohl, A.: Water vapor $\delta^2\text{H}$ and $\delta^{18}\text{O}$ measurements using off-axis
1176 integrated cavity output spectroscopy, *Atmos. Meas. Tech.*, 3, 67-77,
1177 <https://doi.org/10.5194/amt-3-67-2010>, 2010.

1178 Thompson, L.G., Davis, M.E., Mosley-Thompson, E., Beaudon, E., Porter, S.E.,
1179 Kutuzov, S., Lin, P.N., Mihalenko, V.N., and Mountain, K.R.: Impacts of
1180 Recent Warming and the 2015/2016 El Niño on Tropical Peruvian Ice Fields, *J.*
1181 *Geophys. Res. Atmos.*, 122, 12,688-12,701,
1182 <https://doi.org/10.1002/2017JD026592>, 2017.

1183 Tremoy, G., Vimeux, F., Mayaki, S., Souley, I., Cattani, O., Risi, C., Favreau, G., and
1184 Oi, M.: A 1-year long $\delta^{18}\text{O}$ record of water vapor in Niamey (Niger) reveals
1185 insightful atmospheric processes at different timescales, *Geophys. Res. Lett.*,

1186 39(8), 805, <https://doi.org/10.1029/2012GL051298>, 2012.

1187 Thurnherr, I. and Aemisegger, F.: Disentangling the impact of air–sea interaction and
1188 boundary layer cloud formation on stable water isotope signals in the warm
1189 sector of a Southern Ocean cyclone, Atmos. Chem. Phys., 22, 10353-10373,
1190 https://doi.org/10.5194/acp-22-10353-2022, 2022.

1191 Thurnherr, I., Hartmuth, K., Jansing, L., Gehring, J., Boettcher, M., Gorodetskaya, I.,
1192 Werner, M., Wernli, H., and Aemisegger, F.: The role of air–sea fluxes for the
1193 water vapour isotope signals in the cold and warm sectors of extratropical
1194 cyclones over the Southern Ocean, Weather Clim. Dynam., 2, 331-357,
1195 https://doi.org/10.5194/wcd-2-331-2021, 2021.

1196 Thurnherr, I., Kozachek, A., Graf, P., Weng, Y., Bolshiyanov, D., Landwehr, S., Pfahl,
1197 Schmale, J., Sodemann, H., Steen-Larsen, H.C., Toffoli, A., Wernli, H., and
1198 Aemisegger, F.: Meridional and vertical variations of the water vapour isotopic
1199 composition in the marine boundary layer over the Atlantic and Southern Ocean,
1200 Atmos. Chem. Phys., 20, 5811-5835, https://doi.org/10.5194/acp-20-5811-2020,
1201 2020.

1202 Uemura, R., Matsui, Y., Yoshimura, K., Motoyam, H., and Yoshida, N.: Evidence of
1203 deuterium excess in water vapor as an indicator of ocean surface conditions, J.
1204 Geophys. Res. Atmos., 113, D19114, <https://doi.org/10.1029/2008JD010209>,
1205 2008.

1206 Villiger, L., and Aemisegger, F.: Water isotopic characterisation of the cloud–circulation
1207 coupling in the North Atlantic trades – Part 2: The imprint of the atmospheric
1208 circulation at different scales, Atmos. Chem. Phys., 24, 957-976,
1209 <https://doi.org/10.5194/acp-24-957-2024>, 2024.

1210 Vimeux, F., Tremoy, G., Risi, C., and Gallaire, R.: A strong control of the South
1211 American SeeSaw on the intra-seasonal variability of the isotopic composition
1212 of precipitation in the Bolivian Andes, Earth. Planet. Sci. Lett., 307, 47-58,
1213 <https://doi.org/10.1016/j.epsl.2011.04.031>, 2011.

1214 Wallace, J.M., and Hobbs, P.V.: 3-Atmospheric Thermodynamics, Atmos. Sci., 63-111,

1215 <https://doi.org/10.1016/B978-0-12-732951-2.50008-9>, 2006.

1216 Wang, B.: The Asian monsoon. Springer praxis books, Springer/Praxis Publishing Co,
1217 Berlin, 787 pp., 651-683, 2006.

1218 Webster, P.J., Magana, V.O., Palmer, T.N., Shukla, J., Tomas, R.A., Yanai, M., and
1219 Yasunari, T.: Monsoons: Processes, predictability, and the prospects for
1220 prediction, J. Geophys. Res. Oceans., 103, 14451-14510,
1221 <https://doi.org/10.1029/97JC02719>, 1998.

1222 Worden, J., Noone, D., Bowman, K., Beer, R., Eldering, A., Fisher, B., Gunson, M.,
1223 Goldman, A., Herman, R., Kulawik, S., Lampel, M., Osterman, G., Rinsland,
1224 C., Rodgers, C., Sander, S., Shephard, M., Webster, C., and Worden, H.:
1225 Importance of rain evaporation and continental convection in the tropical water
1226 cycle, Nature, 445, 528-532, <https://doi.org/10.1038/nature05508>, 2007. Xu, T.,
1227 Pang, H., Zhan, Z., Zhang, W., Guo, H., Wu, S., and Hou, S.: Water vapor
1228 isotopes indicating rapid shift among multiple moisture sources for the 2018-
1229 2019 winter extreme precipitation events in southeastern China, Hydrol. Earth
1230 Syst. Sci., 26, 117-127, <https://doi.org/10.5194/hess-26-117-2022>, 2022.

1231 Yao, T., Thompson, L.G., Mosbrugger, V., Zhang, F., Ma, Y., Luo, T., Xu, B., Yang, X.,
1232 Joswiak, D.R., Wang, W., Joswiak, M.E., Devkota, L.P., Tayal, S., Jilani, R., and
1233 Chen, F.: Third Pole Environment (TPE), Environ. Dev., 7, 52-64,
1234 <https://doi.org/10.1016/j.envdev.2012.04.002>, 2012.